Diffusion and Solid State NMR Studies of Structures in Model Biological Membranes

by

Hyo Soon Cho

B. S. in Chemistry, Korea University, 2002

M. S. in Chemistry, Seoul National University, 2004

Submitted to the Graduate Faculty of

Arts and Sciences in partial fulfillment

of the requirements for the degree of

Doctor of Philosophy in Analytical Chemistry

University of Pittsburgh

2011

UNIVERSITY OF PITTSBURGH

ARTS AND SCIENCES

This dissertation was presented

by

Hyo Soon Cho

It was defended on

June 23, 2011

and approved by

David Waldeck, PhD, Professor, Department of Chemistry

Sunil Saxena, PhD, Associate Professor, Department of Chemistry

Patrick van der Wel, PhD, Assistant Professor, Department of Structural Biology

Dissertation Advisor: Megan M. Spence, PhD, Assistant Professor, Department of Chemistry

Diffusion and Solid State NMR Studies of Structures in Model Biological Membranes

Hyo Soon Cho, PhD

University of Pittsburgh, 2011

We studied the structures in model biological membranes using solid state NMR and NMR diffusion microscopy. We have created a stable bicelle system containing cholesterol, unsaturated and saturated lipids, capable of forming micron-scale lipid domains and suitable for structural biology studies of membrane proteins. The domains were observed by measuring time-dependent diffusion constants reflecting restricted diffusion of the lipids within micron-scale regions of the bicelles. We observed the correlation of bilayer structure of diverse bicelle systems with their alignment capability, using ^{31}P NMR to measure the density of perforations in the bilayer as a function of bicelle alignment. We found a critical density for optimal bicelle alignment, applicable to bicelles of different lipid compositions. We were able to measure the effect of the perforation density on micron-scale domain formation in lipid bilayers. The perforations redistributed line active lipids within the bilayer, affecting the bulk line tension of the lipid domain. This work demonstrated that membrane topology can control domain formation.

TABLE OF CONTENTS

LIST OF TABLES

LIST OF FIGURES

PREFACE

First of all, I would like to express my sincere thanks to my advisor, Dr. Megan M. Spence, for providing me with the opportunity to work on very exciting research projects. She always showed me strong confidence and encouraged me to perform to the best of my abilities with her endless patience throughout my graduate research. I truly appreciate the time and effort that she has devoted to helping me to earn my PhD degree. It is my great honor to become the very first graduate student who earns the PhD degree with Dr. Spence as a research advisor. I wish the best and the lasting happiness for Megan, Paul, and their adorable children, John and Toby.

I am deeply grateful to Dr. David Waldeck, Dr. Sunil Saxena, and Dr. Patrick van der Wel, for being my committee members, for their help as well as encouragement.

To the past and present members of the Spence group, I would like to express my thanks to all of them for their help during my time at Pittsburgh. I hope Lauren, Kevin and Bocheng come up with great results in their research projects, to contribute the ongoing and exciting research in the Spence lab.

I would like to give great thanks to my love, Jung-hyun Park. We promised to earn PhD when we arrived in States, now our dreams have come true. Without his support, I would have not made it possible. Finally, I would like to thank and express my endless love to my grandmother, my parents, my parents-in-law, brother-in-law, my brother and his wife in Korea.

1.0 INTRODUCTION

1.1 SOLID STATE NMR

Solid state nuclear magnetic resonance (NMR) spectroscopy is a promising tool for the structural study of membrane proteins and biophysical investigation of membranes [1-7]. In contrast to X-ray crystallography, which requires pure crystals with high quality and large size [8], and solution state NMR, which requires molecules to be solubilized and tumbling rapidly in particular solvents, solid state NMR is useful for collecting information about systems like biological membranes that lack crystalline order and cannot be solubilized. Solid state NMR features anisotropic interactions like dipole-dipole coupling and chemical shift anisotropy, which offers detailed structural information (Figure 1) [9, 10]. Solid state NMR can also exhibit the well-resolved spectrum of solution state NMR, exploiting the chemical shift information familiar to chemists [11-13]. With the ability to measure anisotropic interactions, solid state NMR is a useful tool for determining the structures and describing the dynamics of membranes and membrane proteins. Therefore, we studied membrane properties such as phase transitions and the alignment range and morphology of our model membranes, using ^{1}H and ^{31}P spectra obtained with solid state NMR.

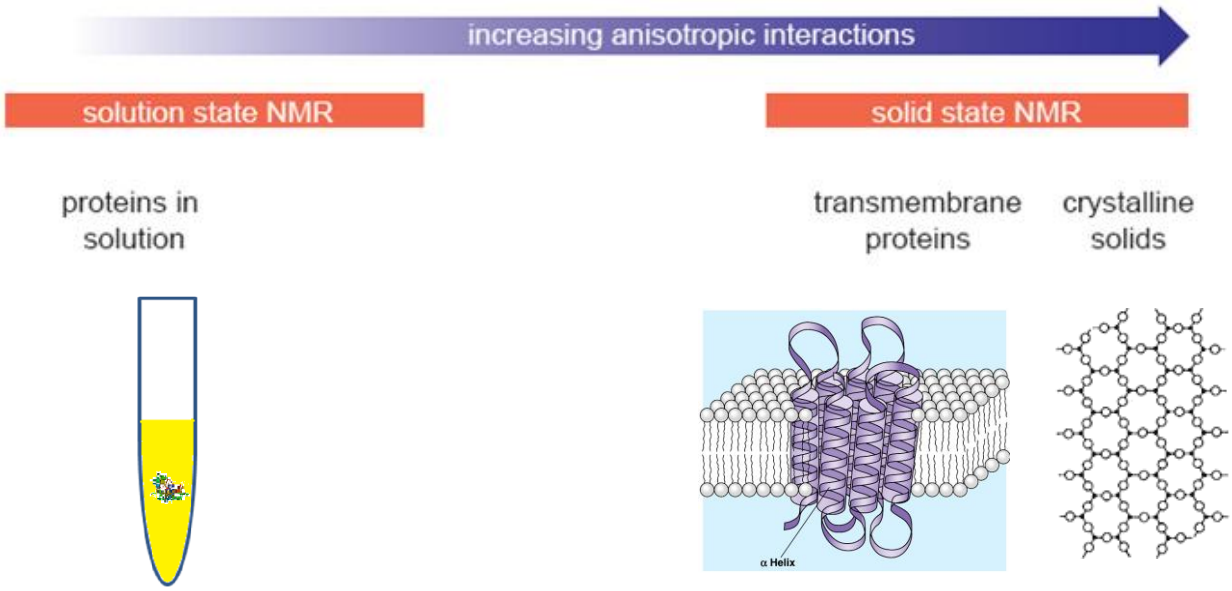

Figure 1. NMR measurement according to the dynamics of sample. Solid state NMR is a useful tool to observe the dynamics and structures of lipid membrane by measuring anisotropic interactions.

1.1.1 ^{31}P NMR SPECTRUM DOMINATED BY CHEMICAL SHIFT ANISOTROPY

Solid-state ^{31}P NMR spectroscopy is a useful method to collect structural information on phospholipid membranes, because the presence of a single phosphorus atom for each lipid leads to a simple spectrum. In addition, the spectrum is dominated by chemical shift anisotropy, giving useful information about the orientation and dynamics of the phosphorus atom (and lipid head group) with respect to the external magnetic field. Dipolar coupling, another feature observable in solid state NMR, is not important for ^{31}P NMR of the membrane because of the low natural abundance of nearby carbons, the low ^{31}P gyromagnetic ratio and the long distance between ^{31}P-^{1}H and ^{31}P-^{13}C. The chemical shift anisotropy tensor can be described using the parameters isotropic chemical shift σ_{iso} and anisotropy σ_{aniso} [9].

$$\sigma_{zz} = \sigma_{iso} + \sigma_{aniso\,,zz}\,\frac{1}{2}(3cos^2\beta - 1) \tag{1}$$

$$\sigma_{iso} = \frac{\sigma_{xx} + \sigma_{yy} + \sigma_{zz}}{3} \tag{2}$$

Here, σ_{xx}, σ_{yy} and σ_{zz} are components of the chemical shift anisotropy tensors. β is the angle between the local bilayer normal and external magnetic field [14].

The chemical shift information about the orientation and dynamics of the lipid head group can clearly show the phase of the lipid aggregation. Figure 2 shows the ^{31}P spectra of vesicles, oriented bilayers and micelles. Figure 2a shows the vesicles with a powder distribution of lipids, reflecting all possible orientations in the chemical shift spectrum. More phospholipids in vesicles are oriented perpendicular to the magnetic field (β = 90°) because of the spherical

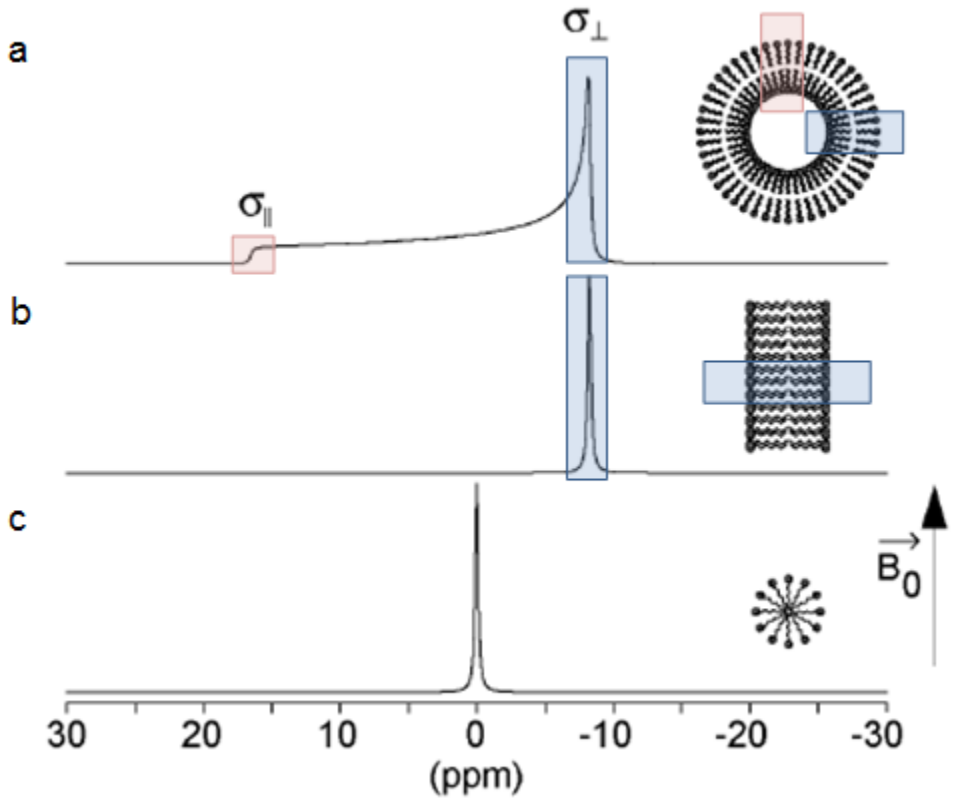

Figure 2. Comparison of ^{31}P spectra of vesicle, bilayer and micelle: (a) dispersion of slow tumbling vesicles, (b) bilayers perfectly aligned perpendicular to magnetic field, (c) rapid tumbling micelles in solution [14].

surface area. Thus, chemical shielding for phospholipids perpendicular to the external magnetic field ($\sigma_{\perp} = \sigma_{zz}$ ($\beta = 90°$)) shows the most intense peak. On the other hand, there are few phospholipids at the poles of the vesicles parallel to magnetic field ($\sigma_{\parallel} = \sigma_{zz}$ ($\beta = 0°$)) and they show very low intensity. Other phospholipids at various angles have various σ_{aniso} values so that the spectrum shows a powder pattern and chemical shift anisotropy as a result of their various orientations. Figure 2b indicates the ^{31}P spectrum of oriented membranes, which are perpendicular to the external magnetic field. The ^{31}P spectrum of micelles exhibits an isotropic spectrum due to the rapid tumbling of the aggregates as shown in Figure 2c. In conclusion, ^{31}P NMR resonance line shapes and shifts are indeed useful for measuring membrane morphology and the orientation of the lipid bilayer with respect to the magnetic field.

Generally, phospholipid bilayers experience several phase transitions with changes in temperature. At low temperatures below T_m, the lipid chain melting point, the lipids exist in the gel phase (L_β), in which hydrocarbon chains are tightly packed. Figure 3c shows the cartoon of a bicelle membrane with the lipids in the gel phase and the corresponding ^{31}P spectrum (bottom). Above T_m, the gel phase becomes the liquid-crystalline phase (L_α). For a bicelle system, this phase can be aligned in the magnetic field and it adopts a planar and Swiss cheese-like morphology. Our lateral diffusion measurements were all carried out in this phase. The L_α phase reflects the phase of the biological membranes, and the uniaxial orientation of the bicelles gives the simplified magnetic resonance spectra of the membrane and proteins in the membrane. Magnetically aligned bicelle spectra show well distinguished narrow phosphorus peaks, in Figure 3b, corresponding to lipids in the bilayer and perpendicular to the bilayer. At the higher temperature T_v, the liquid-crystalline phase changes to vesicles in Figure 3a and ^{31}P spectrum shows that the alignment is lost (top) [15].

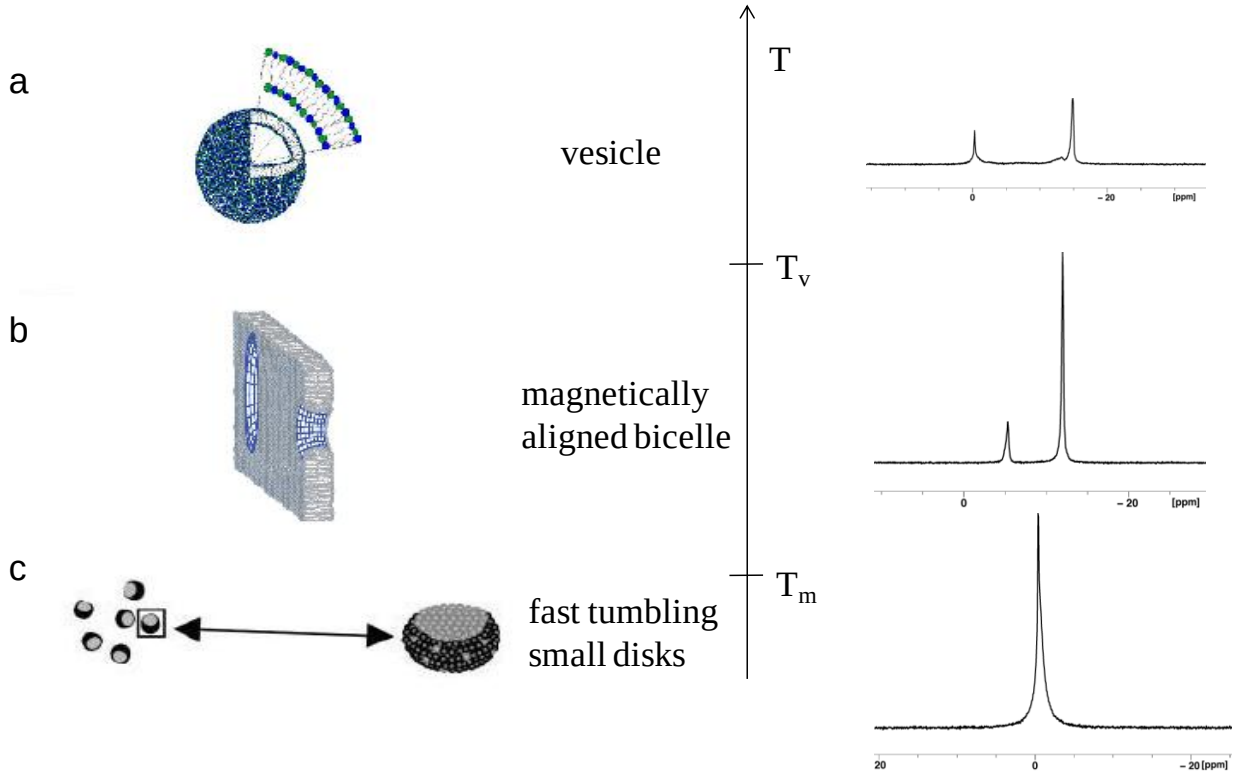

Figure 3. ^{31}P spectra acquired of bicelles in our lab at the main transition temperatures from low to high and corresponding cartoon of the various DMPC/DHPC structures. Right spectra represent gel, aligned bicelle and vesicle phases, as corresponding to the left figures, respectively. This figure was modified from published papers [16, 17].

1.1.2 ^{1}H SPECTRA DOMINATED BY DIPOLAR COUPLING

In contrast to the ^{31}P spectra, ^{1}H NMR of membranes is dominated by dipolar couplings. Dipolar coupling is defined as the interaction of the nuclear magnetic moments of two different nuclear spins, I and S, where the local magnetic field at spin S is affected by spin I. The magnitude of dipolar coupling reflects the internuclear distance, r_{IS}, of two nuclei, their gyromagnetic ratios, γ_I and γ_S, and the angle θ between the external magnetic field, $B_{o,}$ and the internuclear vector of I and S. This can be seen in Eq. (3) and Figure 4a [18]

$$D = \left(\frac{-\hbar\mu_0}{4\pi}\right)\frac{\gamma_I\gamma_s}{r_{IS}^3}(3cos^2\theta - 1)\,, \tag{3}$$

where μ_0 is the permeability of free space ($4\pi \times 10^7$ NA^{-2}), and ħ the Planck constant. Thus, dipolar coupling provides structural information and orientation information about the molecules.

In particular, the proton spectra of solid crystals are not generally collected because of large ^{1}H-^{1}H dipolar coupling (due to the large gyromagnetic ratio, γ_H), which broadens the spectral features, destroying both spectral resolution and signal. Specifically, dipolar couplings of ^{1}H-^{1}H for static crystalline samples are very large with values of ~ 600 kHz [19].

Fortunately, the degree of dynamics experienced by the liquid crystalline biological membrane scales these couplings to thousands of Hz, allowing the use of magic angle spinning (MAS) to retrieve the isotropic ^{1}H spectrum so familiar to chemists. Diffusion experiments especially need peaks of high resolution and large signal, such as isotropic peaks in a solution. This linebroadening issue can be solved by fast spinning at θ = 54.74°, called the "magic angle" [10, 20, 21], which is shown in Figure 4b. When the axis of the rotor is at the "magic angle" and

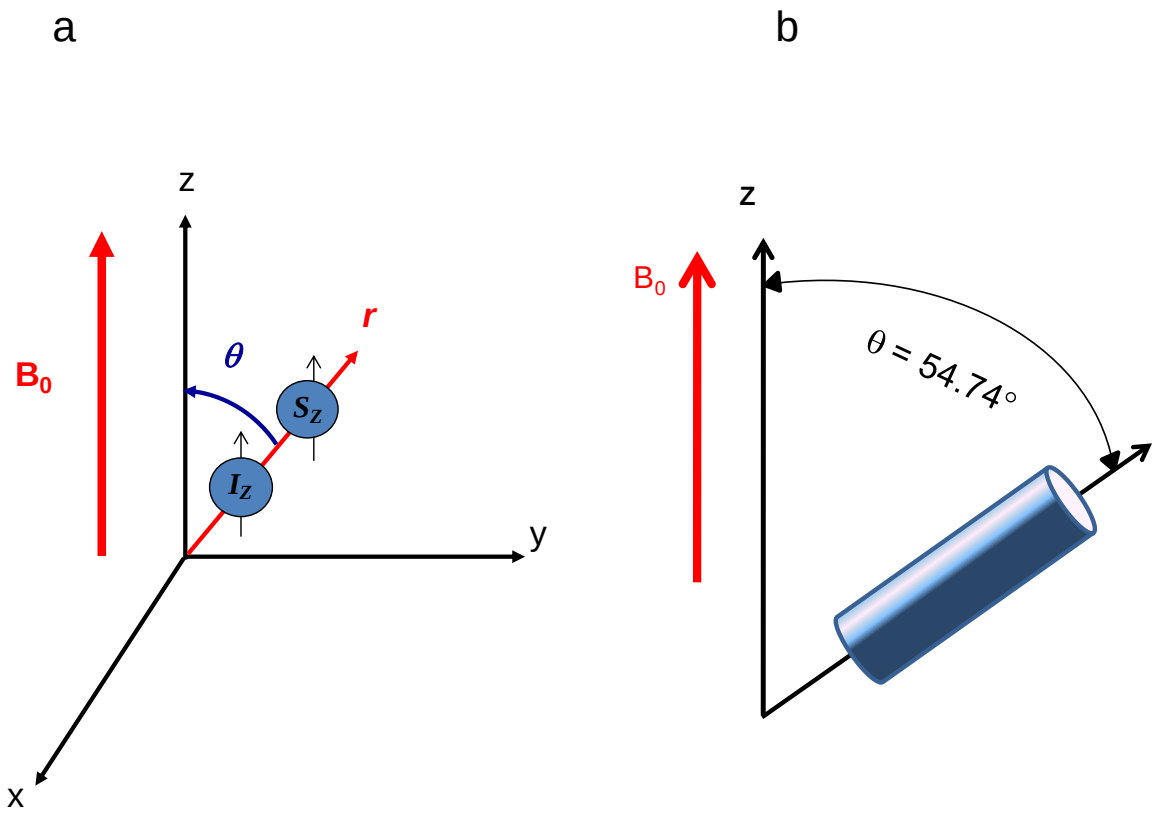

Figure 4. (a) Dipolar couplings between two different nuclear spins. Dipolar coupling gives structural information by considering the internuclear distance and orientation with respect to the external magnetic field. (b) The linebroadening due to dipole-dipole interaction and chemical shift anisotropy can be removed using magic angle spinning. The narrow lineshape of the peak under magic angle spinning allows ^{1}H diffusion NMR measurement on bilayers.

spun fast with a spinning rate larger than the size of spectral features, the dipole coupling tensor is averaged out perpendicular to the spinning axis, and only the component along the spinning axis remains. Because the spinning axis is at the "magic angle", the remaining dipolar coupling is zero. In a solid crystal sample, the current spinning technology (up to 70 kHz) is not fast enough to remove the linebroadening due to large dipolar coupling. In contrast, as lipid membranes are more dynamic than a solid sample, magic angle spinning at lower frequencies than 10 kHz can produce an isotropic ^{1}H spectrum in a biological membrane. Therefore, with our lipid model membranes, we could perform the ^{1}H and ^{31}P NMR diffusion experiment and obtain solution-like isotropic peaks under magic angle spinning.

1.2 NMR DIFFUSION TECHNIQUE: MEASUREMENT OF THE DOMAIN SIZE IN A MEMBRANE

The solid state NMR diffusion technique is widely used to measure the lateral diffusion in a membrane, and it provides essential understanding of membrane structures and biophysical properties of the membrane as well as the intermolecular interaction of the chemical system [22-25]. For example, it could measure lateral diffusion of membrane proteins associated with the membrane [26] and the association constant of a host-guest system with fast exchange [27, 28]. We focused on utilization of NMR diffusion to measure the domain size in our model membranes because of its promise in measuring sub-micron domains beyond the diffraction limit of optical microscopy. Figure 5 indicates the length scales of the domains in biomembranes. Domains in a cell membrane are generally small, 10 - 200 nm, and rich in sphingolipids and cholesterol as they create membrane heterogeneity [29]. The heterogeneity is involved in various

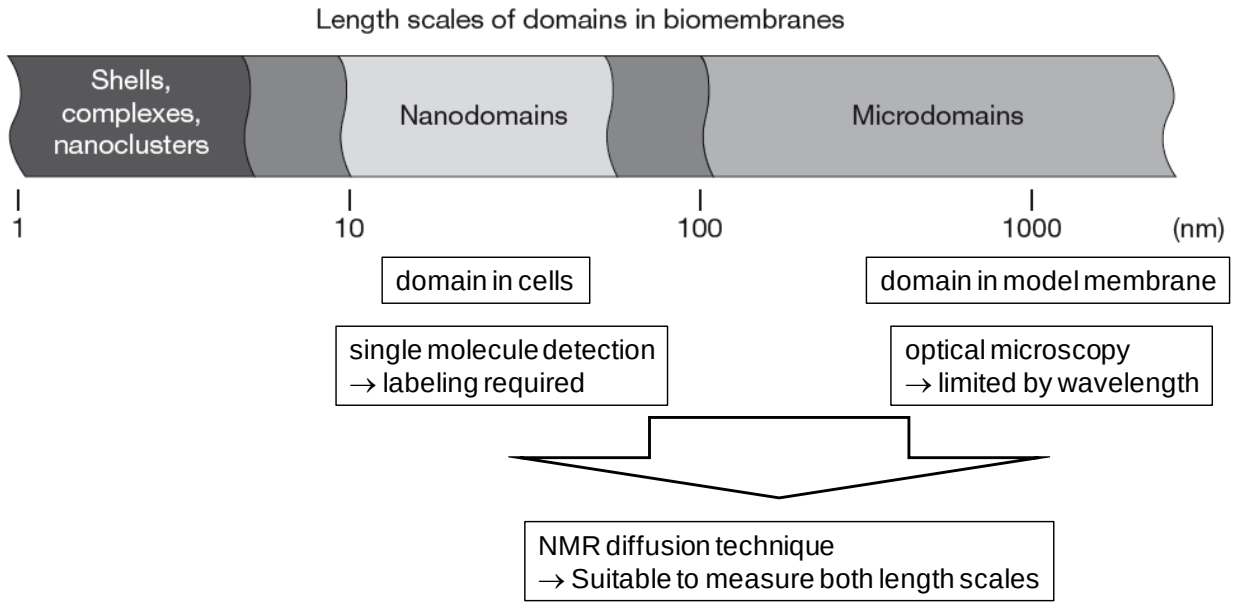

Figure 5. Domain length scales in biomembranes. The NMR diffusion technique can possibly measure both length scales of domains in cell and model membranes. This figure was modified from a published paper [30].

cellular processes like signaling and membrane trafficking [31, 32]. However, it is difficult to observe the domains using optical methods like fluorescence due to their small size [33, 34]. The single molecule detection method could be a breakthrough for measurement, but it also requires the attachment of labels for successful monitoring [35]. Lipid domains in a model membrane have micron-scale sizes much larger than cell membrane domains. Their larger domain sizes can be measured using optical microscopy, but the resolution is limited by the wavelength of light. For domains in both cell and model membranes, the NMR diffusion technique may potentially measure both length scales (vide infra) as its resolution is determined by the gradient strength, an engineering limitation. Lipid domains in both model and cellular membranes are governed by lipid phase separation in mixtures of cholesterol and saturated and unsaturated phospholipids. Thus, even though there is a limitation to representing and explaining cell membrane domains using model lipid domains, biophysical studies of these lipid domains can be used to investigate the interactions of membrane proteins, membrane curvature, and even cytoskeleton with these model domains [34].

1.2.1 STRUCTURE OF MEMBRANE DOMAINS REFLECTED IN LIPID DIFFUSION

Domains are formed by the miscibility of saturated and unsaturated lipids in the presence of cholesterol, as can be seen in Figure 6. Domains are the segregated regions of lipid membranes formed due to the immiscibility of liquid-ordered (l_o) and disordered (l_d) phases. Generally lipid bilayers exist in solid-like (gel) states below both T_m, forming tightly packed domains. At that time, lipids are well mixed and there is no phase separation. Between the two lipid chain melting points, long chain saturated lipids with high T_m form a liquid-ordered domain whereas long chain unsaturated lipids with low T_m form a liquid-disordered domain. Cholesterols

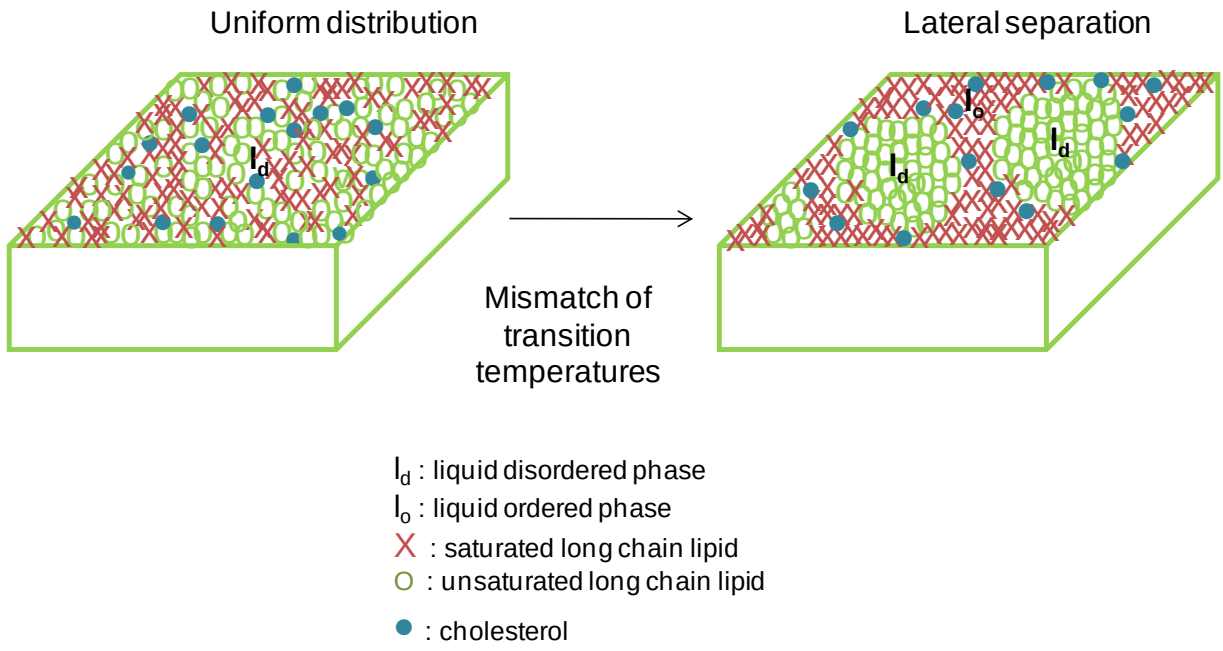

Figure 6. Schematic of lipid domains. Lateral phase separations of the membrane into liquid ordered phase (l_o) enriched in saturated lipid and liquid disordered phase (l_d) domains enriched in unsaturated lipid, are made favorable by the presence of cholesterol.

are incorporated into the l_o domain as promoting the phase segregation [36-39]. We focused on creation of the model membrane which has a lipid composition close to that of a biological cell membrane, and measured domain size using solid state NMR. In addition, in order to test for the presence of the lipid domains and to measure their size, we performed lateral diffusion measurements to see the effect of domain boundaries on lipid diffusion (Figure 7). We expected the diffusion constant of the aligned domain-containing unsaturated bilayer to show different behavior from that of a conventional saturated lipid bilayer. The presence of lipid domains leads to an apparent decrease in the diffusion constant of lipids in the domains as they encounter boundaries during their diffusion, as well as making the apparent diffusion constant dependent on the diffusion time. In contrast, membranes without any domains show a diffusion constant which would not be affected by boundaries and would be constant as the diffusion time is varied.

1.2.2 NMR DIFFUSION MEASUREMENTS TO MEASURE LIPID DOMAINS IN A MODEL MEMBRANE

The maximum resolution of optical microscopy in observing membrane structure is limited by the wavelength of light used. On the other hand, the spatial resolution of NMR diffusion microscopy measurement is only limited by gradient strength, so that in the presence of strong gradient, this technique can theoretically measure small domains below 100 nm [40]. Therefore, in order to measure the lipid diffusion coefficient and domain size, we used a stimulated echo pulsed field bipolar gradient using a WATERGATE sequence under magic angle spinning as shown in Figure 8 [41].

Here, the location of spins is encoded by the first gradient pulse of duration δ and amplitude g and decoded by the second gradient pulse [22] after the spins diffuse for time Δ.

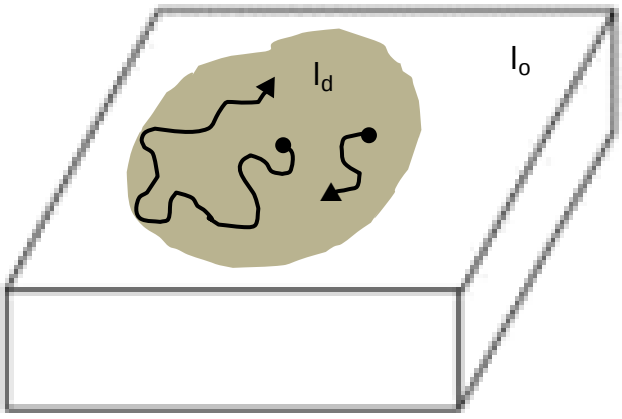

l_d : liquid disordered phase
l_o : liquid ordered phase

Figure 7. Boundary effect on diffusion measurement. Disruption of the diffusion reflects the existence of a boundary of the lipid domain and its size. Over a short diffusion time (short path), diffusion is uninterrupted. Over a long diffusion time (long path), diffusion would be interrupted by the boundaries of lipid domains, giving a smaller apparent diffusion constant.

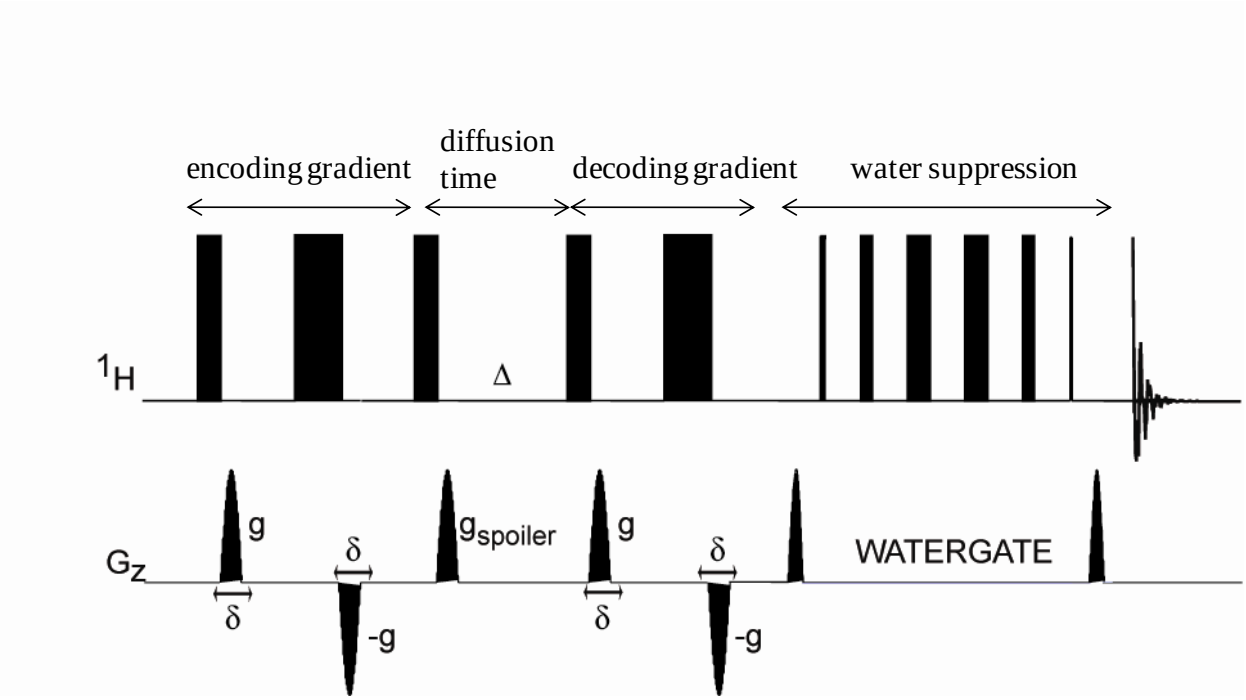

Figure 8. 1D sequence using stimulated echo bipolar pulsed field gradient with WATERGATE sequence. During the first period, spin positions are encoded along the z direction, which is the applied magnetic field direction by gradient pulse of duration δ with a π rf pulse. This spin magnetization is stored along the z direction during Δ, diffusion time, and during the third period, the spin positions are decoded. If spin positions are changed after the diffusion time, incomplete spin refocusing will occur. Thus, the resulting echo signal will be attenuated by the spin motion to different positions. WATERGATE is used to suppress the water peak so that other lipid peaks are well observed.

During the diffusion time, magnetization is stored along the z direction, because the transverse relaxation time for the lipids is very short. Therefore, diffusion time, Δ, is limited only by longitudinal relaxation time and can be up to 1 s. We used $g_{spoiler}$ to destroy any magnetization left by pulse length imperfection. The intensity of the signal is decreased as the spin positions are changed after diffusion time because the encoding and decoding gradients give imperfect rephasing resulting from the spin motion. Eq. (4) exhibits the stimulated echo attenuation I (G,Δ) after spin positions change from z_1 to z_2 [42].

$$I(G,\Delta) = \int_{-\infty}^{\infty} P(z,\Delta)\, cos(\gamma\delta G z)\, dz \tag{4}$$

Here, $P(z, \Delta)$ is the probability that a spin is displaced from z_1 to z_2 after diffusion time Δ ($z = z_2 - z_1$), G gradient amplitude, γ gyromagnetic ratio, δ gradient pulse duration, and Δ diffusion time. We assume that $P(z, \Delta)$ is controlled by a random walk, resulting in Gaussian distribution as shown in Eq. (5).

$$P(z,\Delta) = \pi^{1/2}\langle x^2\rangle^{1/2}\exp(-z^2/\langle x^2\rangle) \tag{5}$$

$\langle x^2\rangle^{1/2}$ is the mean square displacement of spins from their initial places and D is the experimental diffusion constant in Eq. (6).

$$\langle x^2\rangle^{1/2} = \sqrt{4D\Delta} \tag{6}$$

With the assumption of a Gaussian spin distribution, Eq. (5) is able to be written as Eq. (7).

$$\frac{I}{I_0} = \exp(-\gamma^2\delta^2 g^2 D\Delta)\ , \tag{7}$$

where I and I_0 are the signal intensity in the presence and absence of the gradient, respectively. To extract the diffusion coefficient from the results, we used the Stejskal and Tanner equation [43], written as Eq. (8), a rearrangement of Eq. (7).

$$ln\left(\frac{I}{I_0}\right) = -\gamma^2\delta^2 g^2 D\Delta = -kD, \tag{8}$$

where k is a function of the following experimental parameters: gradient duration δ, gradient amplitude g, and diffusion time Δ.

1.2.3 RESOLUTION LIMIT OF NMR DIFFUSION MICROSCOPY

In order to measure D, appropriate k should be sampled to induce good signal attenuation leading to precise measurement of D. Therefore, we required $k_{max} \cdot D \cong 1$, where k_{max} is the k value at full gradient strength. This requirement leads to the resolution limit of the diffusion microscopy technique, as k_{max} imposes a minimum resolution, r_{min}. When we measure the sub-micron-scale domain size, the measurement should be performed at a short diffusion time. If the

diffusion time, Δ, must be short, then g_{max} should be large or δ should be long to reach $k_{max,}$ satisfying the requirement of $k_{max} \cdot D \cong 1$. Therefore, r_{min} can be given by Eq. (9)

$$r_{min} = \frac{2}{\gamma \cdot \delta \cdot g_{max}} , \tag{9}$$

where r_{min} is the limit of domain measurement capability, γ the gyromagnetic ratio, δ the gradient duration, and g_{max} the maximum gradient strength. This equation indicates that a shorter δ and stronger g_{max} can increase the spatial resolution of the measurement. With our current gradient of 1.5 T/m, a diffusion measurement of ^{1}H can resolve domains as small as 1.5 μm. Increasing the gradient to 25 T/m could theoretically increase our domain resolution to 30 nm, potentially making diffusion-based NMR microscopy a valuable method to observe small lipid domains.

1.2.4 MODELS FOR DIFFUSION IN BILAYER

Diffusion in bilayer can be classified by the type of mean-square displacement as seen in Figure 9 [44]. The graph in Figure 9 shows the types of displacement when displacements are normal, anomalous, directed and confined, respectively. Among them, in the confined displacement, the diffusion describes the restriction with in a circular sample. When displacement is observed at long diffusion time, the displacement is confined in the domain and the plateau of the displacement indicates the size of the domain as you can see in Eq. (10) [44]

$$\langle x^2 \rangle^{1/2} = \sqrt{\langle x^2 \rangle_0 [1 - e^{-t/\tau}]} . \tag{10}$$

`

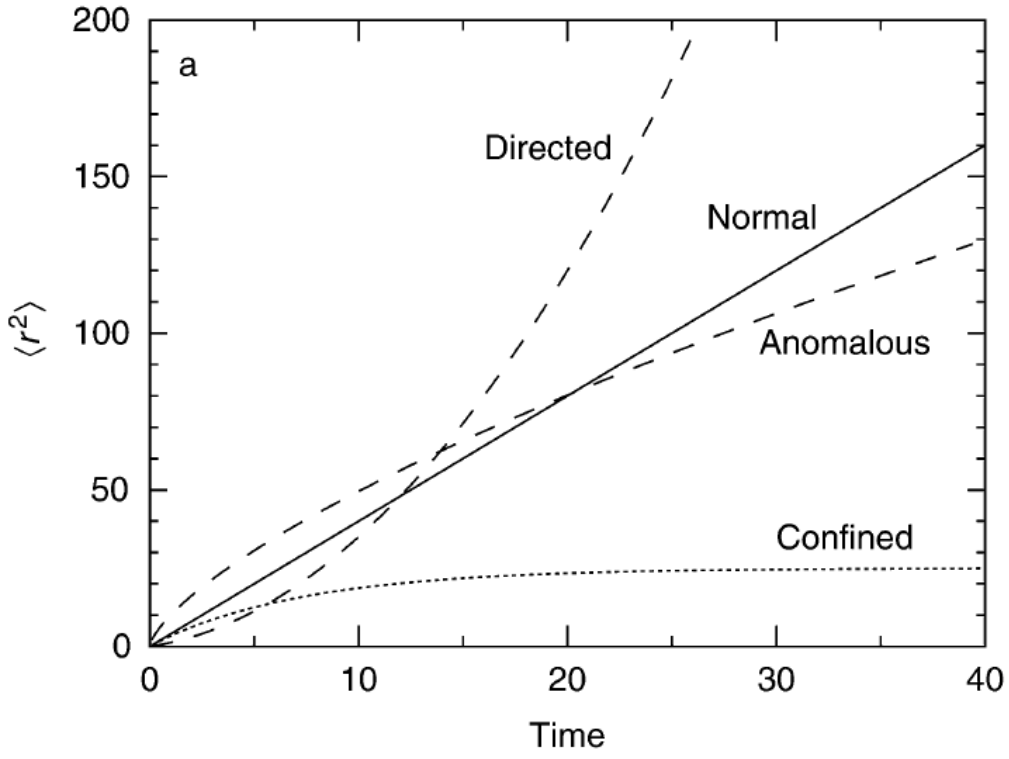

Figure 9. Models for diffusion in bilayer. This graph was taken from the reference [44].

The confined diffusion also can be borrowed from the diffusion on spherical sample [45]

$$\langle x^2 \rangle^{1/2} = r\, sin\left(\frac{\sqrt{4D_{true}\Delta}}{r}\right). \tag{11}$$

This displacement also can express the time-dependent diffusion, showing the plateau which indicates the confined diffusion. Moreover, both diffusions in circular and spherical system show no displacements when t = 0, and at small t, the displacements are proportional to the square root of diffusion time and diffusion constant.

2.0 LIPID DOMAINS IN BICELLES CONTAINING UNSATURATED LIPIDS AND CHOLESTEROL

This work, written in collaboration with Johnna L. Dominick, and Megan M. Spence, has been published in Journal of Physical Chemistry, B, 2010, 114, 9238–9245.

2.1 ABSTRACT

We have created a stable bicelle system capable of forming micron-scale lipid domains that orient in a magnetic field, suitable for structural biology determination in solid-state NMR. The bicelles consisted of a mixture of cholesterol, saturated lipid (DMPC), and unsaturated lipid (POPC), a mixture commonly used to create domains in model membranes, along with a short chain lipid (DHPC) that allows formation of the bicelle phase. While maintaining a constant molar ratio of long to short chain lipids, q = ([POPC]+[DMPC])/[DHPC] = 3, we varied the concentrations of the unsaturated lipid, POPC, and cholesterol to observe the effects of the components on bicelle stability. Using ^{31}P solid-state NMR, we observed that unsaturated lipids (POPC) greatly destabilized the alignment of the membranes in the magnetic field while cholesterol stabilized their alignment. By combining cholesterol and unsaturated lipids in the bicelles, we created membranes aligning uniformly in the magnetic field, despite very high concentrations of unsaturated lipids. These bicelles, with high concentrations of both cholesterol

and unsaturated lipid, showed similar phase behavior to bicelles commonly used in structural biology, but aligned over a wider temperature range. Domains were observed by measuring time-dependent diffusion constants reflecting restricted diffusion of the lipids within micron-scale regions of the bicelles. Micron-scale domains have never been observed in POPC/DMPC /cholesterol vesicles, implying that bilayers in bicelles show different phase behavior than their counterparts in vesicles, and that bilayers in bicelles favor domain formation.

2.2 INTRODUCTION

Membrane domains are hypothesized to organize the cell membrane by creating a lateral phase separation of lipids capable of sorting membrane proteins and regulating their activity [46]. Lipid domains have been demonstrated in model membranes formed from a ternary mixture consisting of the following components: unsaturated lipids, saturated lipids, and cholesterol, and are considered a model system for membrane domains. Based on model membranes, membrane domains are described as in the liquid ordered (l_o) state, and show distinctly different structural and dynamical properties than the liquid disordered (l_d) state common in cellular membranes. These structural and dynamical differences are important to the function of membrane domains in modulating protein structure and accessibility [47], but molecular details of the interaction between domains and proteins are lacking.

Model membranes containing lipid domains have not been used for membrane protein structural biology, mainly because of the severe constraints that the techniques place on the membrane composition. X-ray crystallography of membrane proteins employs detergents to solvate hydrophobic regions of the protein, or use 3D crystals of lipid bilayers [48]. Solid state

NMR can use intact lipid bilayers, but many experiments are designed for uniaxially aligned membrane samples, either mechanically aligned between glass slips, or aligned in the magnetic field [49]. The alignment of these membranes is very sensitive to membrane composition, and has been optimized for membranes composed of saturated phosphatidylcholines. For example, when the molar ratio of short and long chain lipid is altered, the bilayer structure and its alignment are varied [16].

The molecular composition of the membrane affects structural properties like membrane thickness and flexibility [50], dynamic properties like membrane fluidity [51], and the formation of phases like lipid domains [38, 52, 53]. Hydrophobic matching and membrane thickness can affect the activity of membrane proteins [54, 55] and membrane composition can modulate membrane protein function [56-58]. Cholesterol has been shown to control the structural interactions between some antimicrobial peptides and membranes [59]. Lipid domains are thought to be thicker than the surrounding membrane [60] and show slower lipid diffusion in measurements of model membranes [61], but the effect of these membrane structural differences on protein structure has not been studied and is unknown.

Bicelles are model membranes well suited to magnetic resonance studies of membrane protein structure because of their ability to orient in a magnetic field [62], and they have been used in most NMR structural studies of transmembrane proteins [17, 49, 63-68]. However, like most model membranes, bicelles usually consist solely of saturated chain phosphatidylcholines, with a long chain lipid forming the bilayer and a short chain lipid solvating any perforations in the bilayer (Figure 10). Historically bicelles are regarded as disk shape, but the appropriate explanation for the bicelle alignment [69], and lateral diffusion experiment results [70] demonstrated that bicelle has the perforated and extended lamellar shape instead of disk shape.

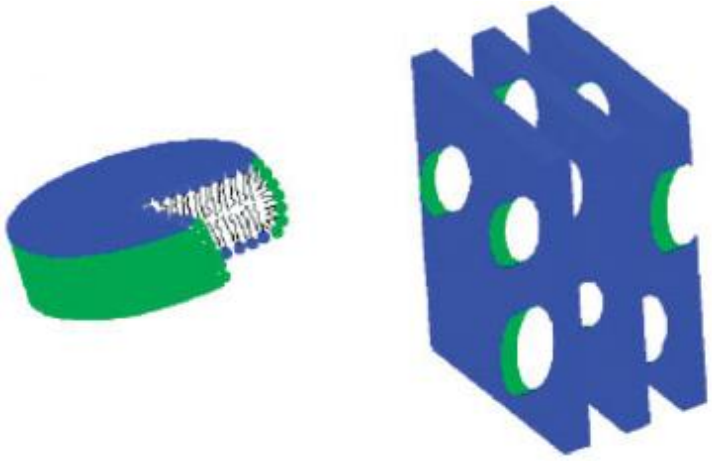

Figure 10. Schematic of bicelles. Left : The short chain DHPC lipid molecules (in green) occupy the rim of the bicelle and long chain DMPC molecules (in blue) are located on the bilayer plane. Right: When the bicelles coalesce, they have the perforated extended lamellae shape like Swiss cheese [62]. This figure was taken from the reference [62].

Bicelles have been created with small amounts of unsaturated lipids [15, 71], cardiolipin [72, 73], and cholesterol [15, 74, 75]. Unfortunately, the stability and alignment of the bicelles can be greatly affected by even a small change in the membrane composition [15, 17, 71, 76]. ^{31}P NMR can monitor any changes in the morphology of the bicelles caused by the addition of new membrane components, and can measure the stability and alignment of bicelle systems.

Lateral diffusion of lipids is a useful metric of the state of a lipid bilayer [77], and is sensitive to parameters like lipid composition, cholesterol content, and temperature. Pulsed field gradient (PFG) NMR is a well-established tool for measuring the self diffusion constant of lipids in bilayers, relying on magic angle spinning (MAS) [78] or macroscopic orientation of the bilayers at the magic angle [79] to narrow the ^{1}H signals characteristic of anisotropic molecular systems.

Using PFG NMR, distinct diffusion constants have been observed for lipids in the l_o and l_d phases, and the onset of domain formation has been measured for domain forming systems [61, 80, 81]. The size of lipid domains has been measured by using PFG NMR experiments to observe the lipid diffusion behavior as a function of diffusion time, with the time-dependent diffusion constant offering a measure of the length scale of membrane inhomogeneity [82, 83].

2.3 EXPERIMENTAL SECTION

2.3.1 SAMPLE PREPARATION

1,2-dimyristoyl-s*n*-glycero-3-dihexanoyl-s*n*-glycero-3-phosphatidylcholine (DHPC, 99 %) in chloroform, and 1-palmitoyl-2-oleoyl-s*n*-glycero-3-phosphatidylcholine (POPC) in

chloroform were purchased from Avanti Polar Lipids (Birmingham, AL). Lipids were used as purchased without further purification. Cholesterol (ovine wool, > 98 %) in powder form, 4-(2-hydroxyethyl)-1-piperazineethanesulfonic acid (HEPES, ≥ 99.5 %) and sodium azide were purchased from Sigma-Aldrich (Allentown, PA). Deuterium oxide was purchased from Cambridge Isotopes Lab (Woburn, MA).

The lipids were dissolved in chloroform and combined in a molar ratio of 2.6/0.4/1 and 1.5/1.5/1 molar ratios of DMPC/POPC/DHPC with and without 13 mol % cholesterol (calculated with respect to moles of long chain lipids) to create unsaturated bicelles (Figure 11). A conventional bicelle sample (no cholesterol or unsaturated lipids) was composed of DHPC and DMPC dissolved in chloroform with molar ratio, q = [DMPC]/[DHPC], equal to 3.5. The lipid mixtures were placed under a nitrogen gas flow for ~ 20 minutes to remove chloroform and then placed on a vacuum line for at least 4 hours until the sample was reduced to a powder or powder/film mixture. A mixture of 10 % deuterium oxide and water was added to each unsaturated bicelle sample to a concentration of 30 % w/w. A 20 mM HEPES buffer (pH = 7.1) was used to redissolve the conventional bicelle mixture to a concentration of 30 % w/w. Three cycles of the following: heating at 40 °C for 15 min, vortexing for 2 min, cooling at 0 °C for 15 min and again vortexing for 2 min, were performed to form bicelle mixtures.

2.3.2 NMR MEASUREMENT

All spectra were acquired using an 11.7 T magnet with a Bruker Avance console (Bruker Biospin, Billerica, MA) and BCU05 Variable Temperature Control Unit. All sample rotors were 200 μL Bruker 4 mm ZrO_2 magic-angle spinning (MAS) rotors. A 4 mm HXY MAS probe was

DHPC

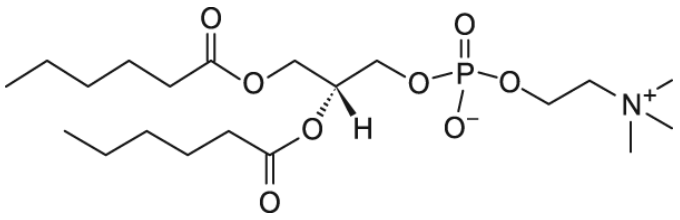

DMPC

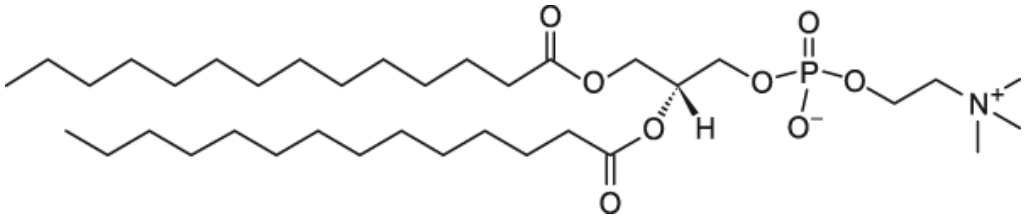

POPC

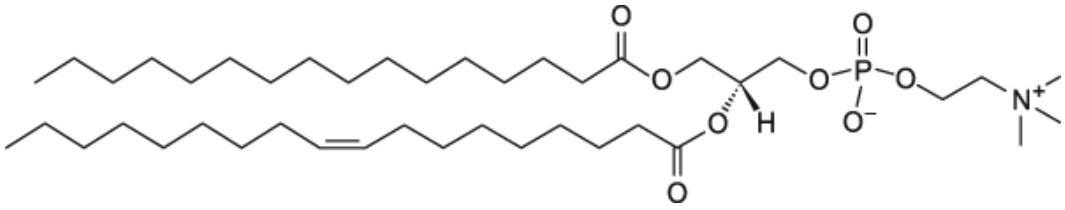

Figure 11. Structures of DHPC (top), DMPC (middle) and POPC (bottom).

used to acquire the ^{31}P NMR spectra. All ^{31}P experiments were performed under static conditions. The variable temperature ^{31}P experiments at 201.98 MHz used FLOPSY at 6 kHz [84] for proton decoupling. The temperature was varied from 273 K to 335 K, in increments of 5 K or 3 K with the sample equilibrating in the probe for 10 to 15 minutes at each temperature. The ^{31}P chemical shifts are referenced to 85 % phosphoric acid.

A high-resolution HCN HR-MAS probe (Bruker Biospin, Billerica, MA) was used to acquire the ^{1}H NMR spectra. All ^{1}H experiments were performed under MAS at 5 kHz in order to obtain isotropic spectra. ^{1}H spectra were acquired after temperature equilibration for 30 minutes. ^{1}H diffusion NMR spectra were recorded at 499.81 MHz with a stimulated echo bipolar pulsed field gradient diffusion experiments using WATERGATE for water suppression [85, 86]. The maximum gradient strength of the magic angle gradient coil was 0.513 T/m. The intensities of the acyl peak (1.2 ppm) were used to calculate the diffusion coefficient. The ^{1}H chemical shifts are referenced to H_2O.

2.4 RESULTS AND DISCUSSION

2.4.1 CREATING MAGNETICALLY ALIGNABLE LIPID DOMAINS

2.4.1.1 ^{31}P SPECTRA AS A METRIC FOR ALIGNMENT AND PHASE

The ^{31}P chemical shift anisotropy of phospholipids is a sensitive probe of the lipid phase and membrane morphology. Aligned bicelles show a characteristic ^{31}P spectrum with two narrow, symmetric lines (Figure 12b) separated by ~ 8 ppm [87]. The chemical shift difference reflects the width of the chemical shift anisotropy pattern of the phosphatidylcholine head group,

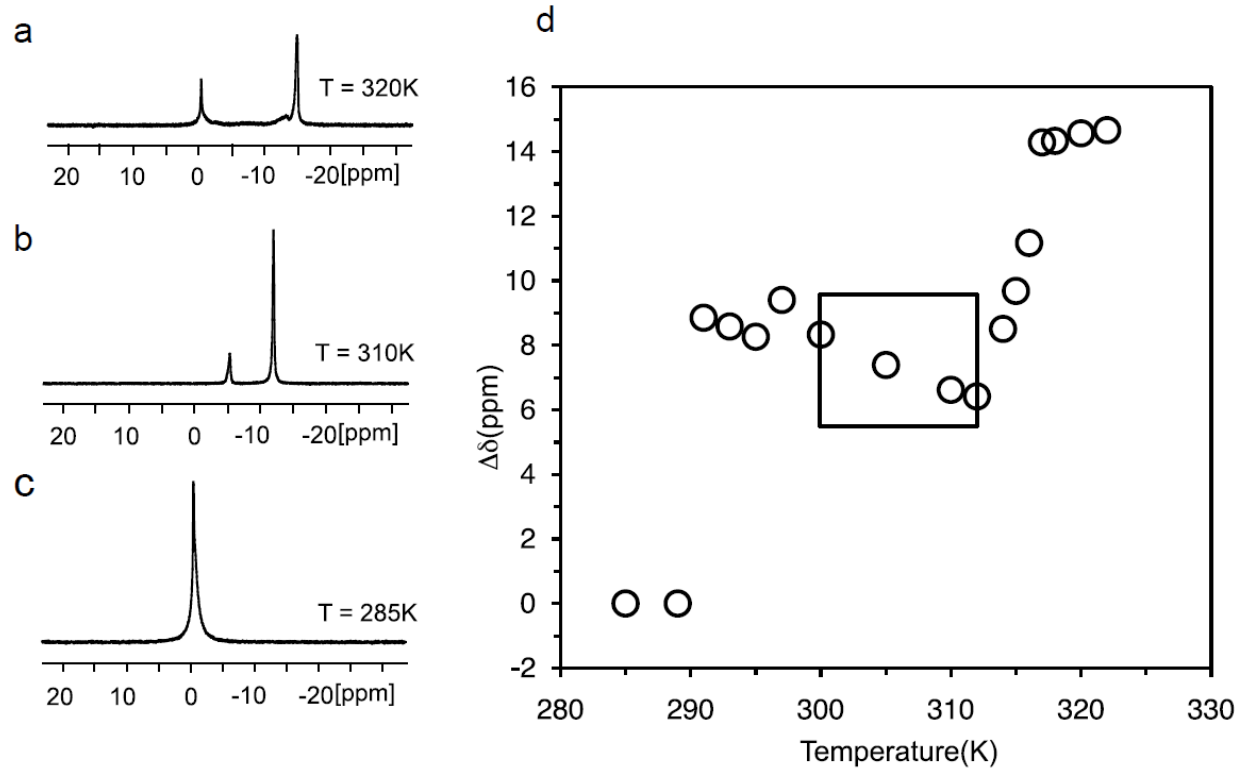

Figure 12. ^{31}P chemical shift difference ($\triangle\delta$) as a measure of bicelle phase. Parts (a)-(c) Vesicle, bicelle, and gel spectra, respectively, of 3.5/1 DMPC/DHPC conventional bicelles. (d) Chemical shift difference increases from 0 ppm (gel phase) to ~ 8 ppm (aligned bicelles) to ~ 15 ppm (vesicles) as temperature of sample is increased. Aligned bicelle phase is present for temperature range defined by box.

and the two peaks arise from the different orientations of lipids in the plane of the membrane and the lipids solvating the holes in the membrane. Three ^{31}P spectra of conventional bicelles (q = 3.5) at different temperatures are shown in Figure 12 to mark the different phases of the lipid mixture.

To summarize the phase behavior of the lipid mixture, we use the chemical shift difference, $\Delta\delta$, between the upfield and downfield peaks in the spectra. In the gel phase at 285 K only one ^{31}P peak is present so the chemical shift difference is 0 ppm (Figure 12c). When the bicelles align at 310 K the two peaks are separated by ~ 8 ppm (Figure 12b) and at 320 K the peaks are approximately 15 ppm apart (Figure 12a), reflecting the transition to vesicles. Plotting $\Delta\delta$ as a function of temperature (Figure 12d) shows the major changes in lipid phase as reflected in the ^{31}P spectrum. The stability and phase behavior of bicelles can be described by the following two parameters: T_{align}, the temperature at which two symmetric peaks appear in the ^{31}P spectrum, and ΔT_{align}, the temperature range over which the bicelles align, indicated by a box in the phase diagram (Figure 12d).

The incorporation of unsaturated lipids or membrane components such as cholesterol increases are necessary for domain formation but can also strongly alter the phase behavior and alignment temperature of a bicelle system. To explore this, we made model membranes containing saturated long chain DMPC and short chain DHPC lipids as well as unsaturated long chain lipid POPC (palmitoyl-2-oleoyl-*sn*-glycero-3-phosphatidylcholine). In addition, in order to look at the effect of cholesterol in the model membrane, we added 13 mol % of cholesterol with respect to long chain lipids into bicelles containing POPC. The phase transitions of the model membranes between different morphologies were detected by solid state ^{31}P NMR spectroscopy and these spectra were used to create phase diagrams like that of Figure 12d.

2.4.1.2 EFFECT OF UNSATURATED LONG CHAIN LIPIDS ON BICELLES

In order to examine the effect of unsaturated long chain lipids on the ability of the membrane to align in the magnetic field, we combined DMPC and DHPC with two different molar amounts of unsaturated lipid. One sample contained a small amount of unsaturated lipid, with molar ratios of 2.6/0.4/1 of DMPC/POPC/DHPC, while another contained equal amounts of saturated and unsaturated long chain lipids (similar to biological membranes [88], with a 1.5/1.5/1 molar ratio of DMPC/POPC/DHPC. Figure 13a,b shows the ^{31}P NMR spectra of the 1.5/1.5/1 DMPC/POPC/DHPC bicelles at main phase transition temperatures between 273 K and 335 K. The spectrum in Figure 13b exhibits the two symmetric lines characteristic of membrane alignment in the magnetic field. The width of the peak at -13.2 ppm likely reflects a distribution in the orientation of the bilayer normal. The spectrum in Figure 13a is consistent with the formation of vesicles above 288 K observed in previous bicelle studies [16]. We also measured ^{31}P NMR spectra of the 2.6/0.4/1 molar ratios of DMPC/POPC/DHPC unsaturated lipid bicelles at temperatures between 273 K and 335 K and created phase diagrams of both model membranes (Figure 13c). The 2.6/0.4/1 DMPC/POPC/DHPC bicelles show that small amounts of unsaturated lipid do not significantly change the alignment temperature, T_{align}, or alignment temperature range, ΔT_{align}, of bicelles. However, bicelles containing equal amounts of saturated and unsaturated long chain lipids aligned at a much lower temperature (T_{align} = 283 K) and aligned over a very small temperature range (ΔT_{align} < 5 K). While the large component of unsaturated lipids makes this bicelle system a good model for cellular membranes, the small alignment range makes it a poor model membrane for structural and biophysical studies.

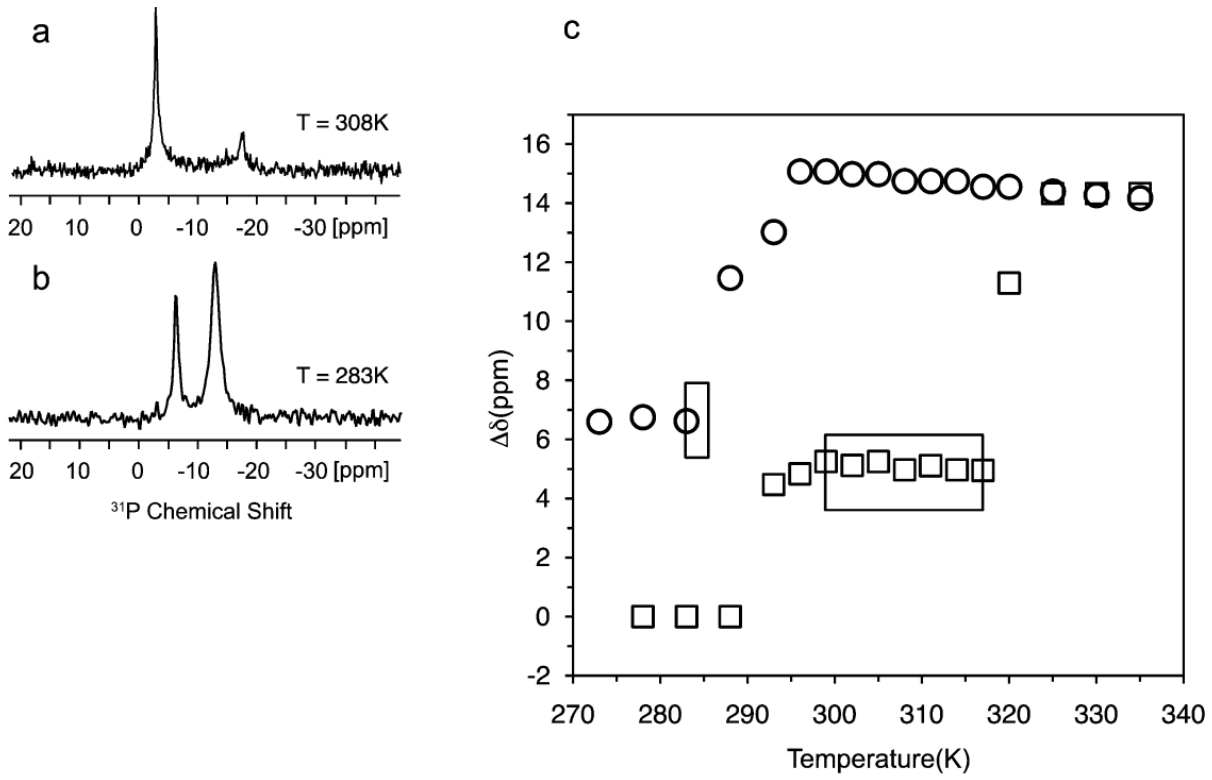

Figure 13. Unsaturated lipids destabilize bicelle alignment. (a),(b) Representative ^{31}P spectra of 1.5/1.5/1 DMPC/POPC/DHPC unsaturated bicelles in vesicle and bicelle phase. (c) 1.5/1.5/1 DMPC/POPC/DHPC bicelles (○) aligned over a small range of ~ 5 K due to the loose chain packing of unsaturated acyl chain. In contrast, 2.6/0.4/1 DMPC/POPC/DHPC bicelles (□) behaved similarly to bicelles without any unsaturated lipids.

2.4.1.3 EFEECT OF CHOLESTEROL ON BICELLES

In order to look at the effect of cholesterol in the model membrane, we added 13 mol % of cholesterol to both unsaturated bicelle samples, reflecting the cholesterol content of the endoplasmic reticulum [89]. Cholesterol is able to restrict the motion of the lipid chains and increase the lipid membrane stability [76], possibly counteracting the effect of unsaturated lipid on the alignment of bicelles [15]. Representative ^{31}P NMR spectra of the 1.5/1.5/1/13 mol % DMPC/POPC/DHPC/cholesterol bicelles are shown in Figure 14a-c for main phase transition temperatures between 273 K and 335 K. At 278 K, the lipids are in the gel state (Figure 14c), transitioning to aligned bicelles at 291 K (Figure 14b), and to vesicles at 315 K (Figure 14a). As shown before, we created a phase diagram of model membranes containing 1.5/1.5/1 DMPC/POPC/DHPC with and without cholesterol, shown in Figure 14d. In the case of the 1.5/1.5/1 DMPC/POPC/DHPC bicelles, cholesterol increased the alignment temperature, T_{align}, from 283 K to 291 K. Among these model membranes, the 1.5/1.5/1/13 mol % DMPC/POPC/ DHPC/cholesterol unsaturated bicelles show the greatest similarity to biological membranes and the greatest stability, reflected in the large alignment temperature range.

2.4.2 RESTRICTED DIFFUSION INDICATES LIPID DOMAINS

The formation of domains has been noted in many systems combining saturated and unsaturated lipids, arising from the different main chain phase transition temperatures, T_m, for the two components [90]. Below the T_m of the unsaturated component, the lipids are miscible in the gel state. In the presence of cholesterol, when the sample is heated above the transition temperature for the unsaturated component, the saturated lipids remain in the ordered state, l_o, but the unsaturated chains form domains of liquid-disordered (l_d) phase [38]. Once the sample is

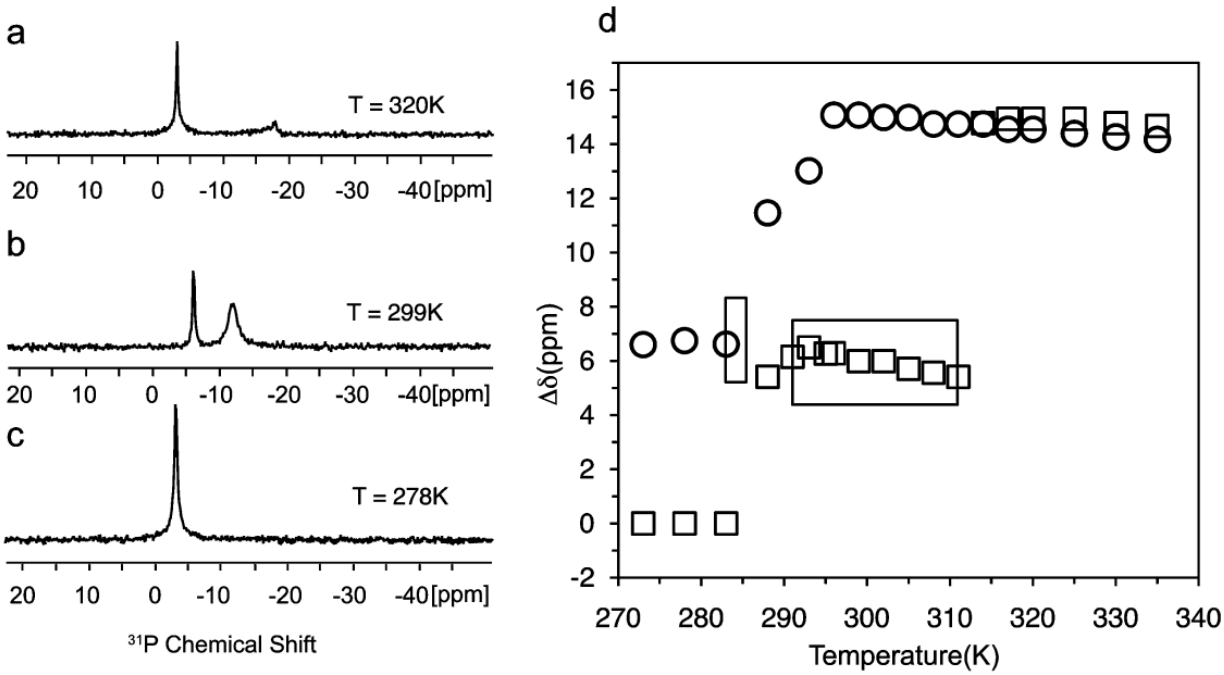

Figure 14. Cholesterol increases alignment temperature range of bicelles. Parts (a)-(c) Representative ^{31}P spectra of 1.5/1.5/1/13 mol % DMPC/POPC/DHPC/cholesterol bicelles in vesicle, bicelle, and gel phase. (d) Bicelles containing unsaturated lipid and cholesterol (□) show increased stability over conventional bicelles and bicelles containing only unsaturated lipid (O) due to condensing effect of cholesterol on the lipid membrane.

heated above the T_m for the saturated lipid, both components are in the l_d phase and mix uniformly again. Domains can be present between the transition temperatures of the two components.

According to this model, domain formation in the 1.5/1.5/1/13 mol % sample is expected between 270 K and 296 K, T_m(POPC) and T_m(DMPC) respectively, and the uniaxial orientation of the domains in the magnetic field would exist between 291 K and 296 K (Figure 15). To measure domain formation in the bicelles, we carried out pulsed-field gradient measurements of the lipid self-diffusion constant. In the absence of domains, the diffusion constant should be independent of the diffusion time of the molecules. If domains are present and restrict the lipid diffusion, the diffusion constant will decrease as the lipid diffusion time increases because the lipid diffusion is confined [78, 83].

2.4.2.1 MEASURING LIPID DIFFUSION

Figure 16a shows the ^{1}H NMR spectrum of 1.5/1.5/1/13 mol % DMPC/POPC/DHPC/ cholesterol bicelles with the choline peak appearing at 3.2 ppm and two acyl chain peaks at 1.2 ppm and 0.8 ppm. The allylic proton peak from POPC appears at 2.0 ppm and WATERGATE has been used to suppress the water peak at 4.7 ppm. For the diffusion measurements, we combined a stimulated-echo pulsed-field bipolar gradient diffusion experiment [41] with water suppression, spinning the sample at the magic angle to obtain well-resolved, isotropic ^{1}H spectra. The acyl peak at 1.2 ppm (marked with an asterisk) was integrated to monitor the lipid signal.
In this experiment, the spin location is encoded by a pair of sine-shaped bipolar gradients of duration δ and amplitude g, bracketing a diffusion time Δ. Diffusion is measured along the direction of the spinning axis with a magic-angle gradient. The intensity of the lipid signal is modulated by the gradient length and amplitude, reflecting the self-diffusion of the lipids. The

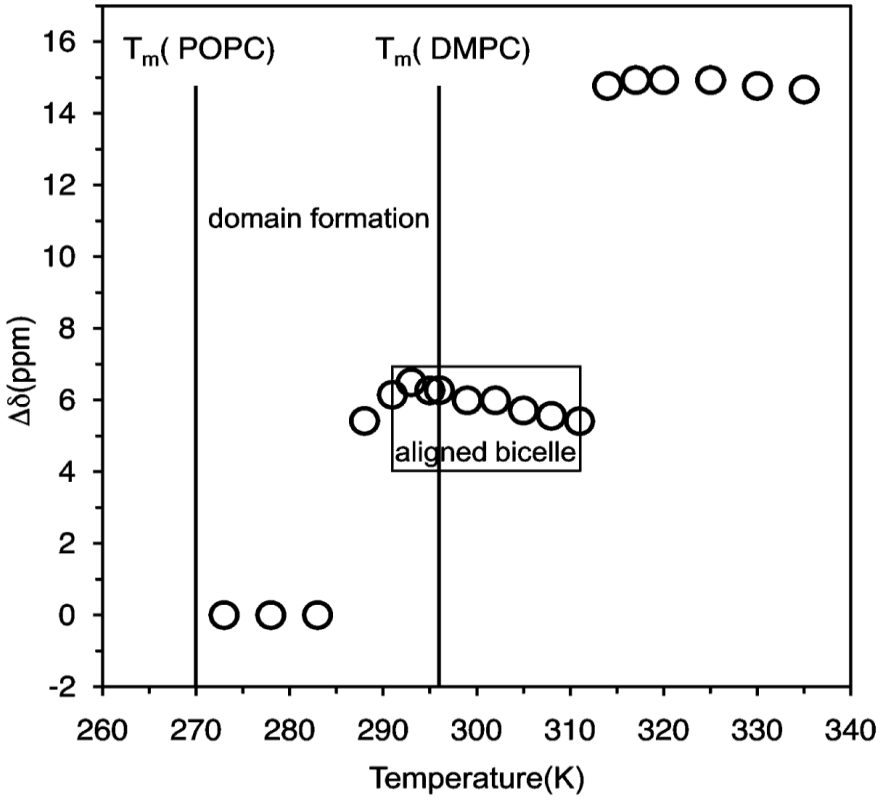

Figure 15. The presence of lipid domains is possible in 1.5/1.5/1/13 mol % molar ratios of DMPC/POPC/DHPC/cholesterol bicelles. Alignment of 1.5/1.5/1/chol DMPC/POPC/DHPC bicelles begins at 291 K, between the two T_m of DMPC (296 K) and POPC (270 K), so domains between 291 K and 296 K should orient in magnetic field.

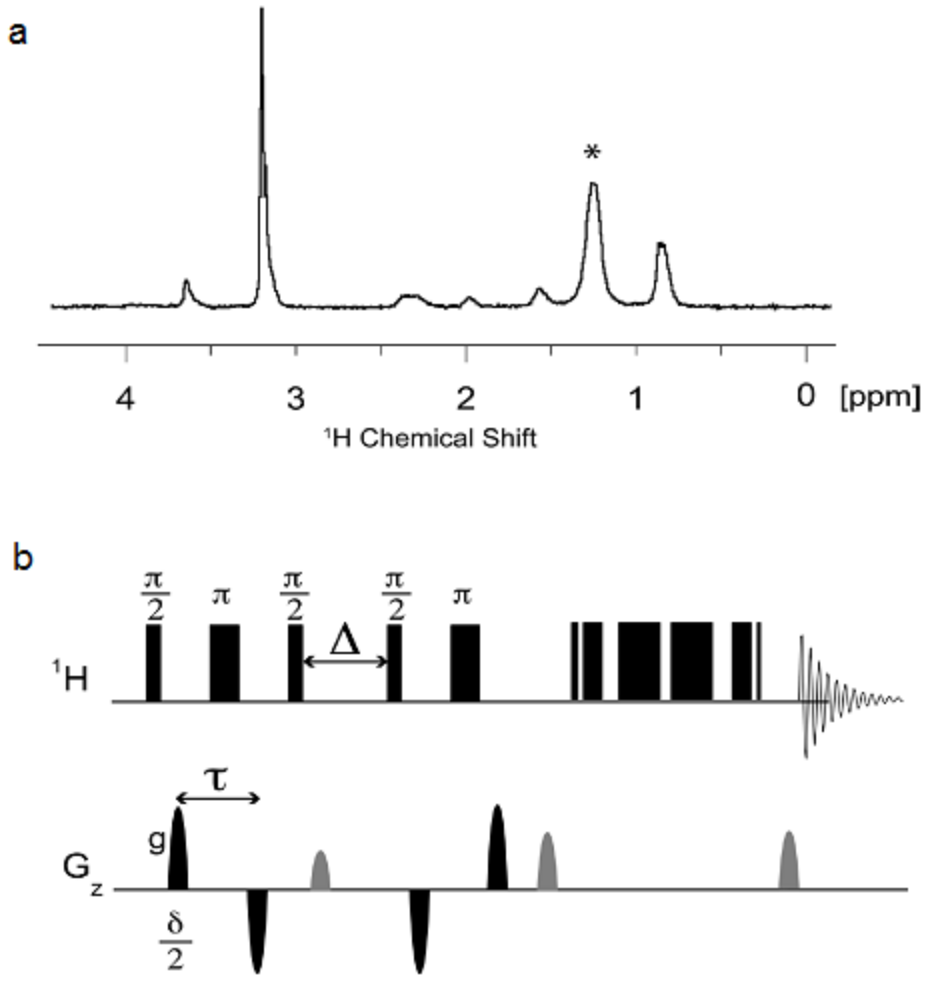

Figure 16. (a) ^{1}H solid-state NMR spectrum of magnetically aligned 1.5/1.5/1/13 mol % DMPC/POPC/DHPC/cholesterol unsaturated bicelles using WATERGATE under magic angle spinning. * acyl peak integrated for diffusion experiment. (b) 1D sequence using stimulated-echo bipolar pulsed field gradient with WATERGATE sequence. During first period, spin positions are encoded along spinning axis by a bipolar gradient pulse of duration δ/2 and amplitude g. This spin magnetization is stored longitudinally during diffusion time, Δ, before the bipolar gradient is applied again.

variation of the signal strength, *I*, with the experimental parameters can be described by the Stejskal Tanner equation [43]

$$\ln\left(\frac{I}{I_0}\right) = -\,g^2\gamma^2\delta^2\left(\Delta - \frac{\tau}{2} - \frac{\delta}{8}\right)\cdot D_{meas} = -k\cdot D_{meas}\ ,$$

(12)

where I_0 is the acyl peak integral in the absence of gradients, τ is the spacing of the bipolar gradient pulses, and γ is gyromagnetic ratio for the observed nucleus (in this experiment ^{1}H). The measured self-diffusion constant, D_{meas}, can be extracted from a plot of ln(I/I_0) versus k (shown in Figure 17). Under the magic angle spinning, the aligning force of the bicelles is lost and the membranes adopt a random distribution of the membrane normal with respect to the magnetic field [91]. Therefore D_{meas} should be multiplied by 3/2 to compensate for the powder pattern to obtain the apparent lateral diffusion constant, D_{app} [26].

In the absence of confinement, lipids show classical diffusion in two dimensions, with a diffusion constant that is independent of diffusion time. Displacement in free diffusion is described by a Gaussian distribution with the root mean square displacement of a lipid increasing with diffusion time, Δ, according to the following equation:

$$\langle x^2\rangle^{1/2} = \sqrt{4D\Delta}$$

(6)

Conventional bicelles containing only DMPC and DHPC are unable to form domains. The long chain lipids in these samples exhibit free diffusion in which the displacement varies linearly with the square root of diffusion time, shown in Figure 18. Each point on this graph represents an apparent diffusion constant measured for a given diffusion time, Δ.

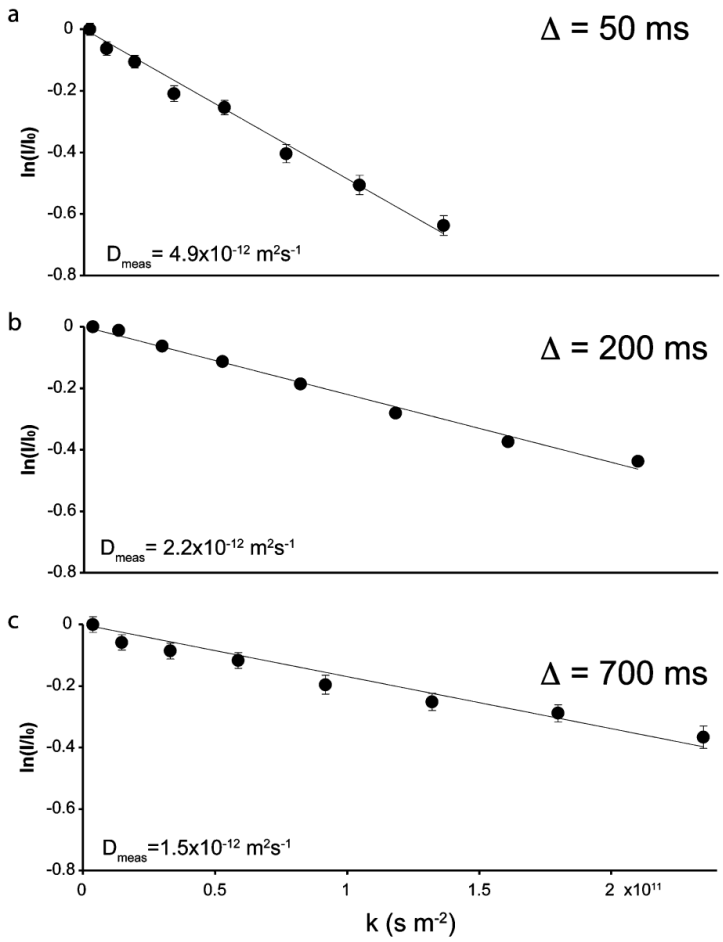

Figure 17. Stimulated-echo intensities are attenuated as gradient strength is increased from ^{1}H NMR spectra of 1.5/1.5/1/13 mol % DMPC/POPC/DHPC/cholesterol bicelles at T = 292 K. As the diffusion time is increased, the diffusion coefficient is decreased due to boundary effect of lipid domains; (a) Δ = 50 ms. (b) Δ = 200 ms. (c) Δ = 700 ms. Gradient strengths are increased from 0.003 Tm^{-1} to 0.168 Tm^{-1}. Error bars reflect the signal to noise ratio of the acyl peak (±2σ).

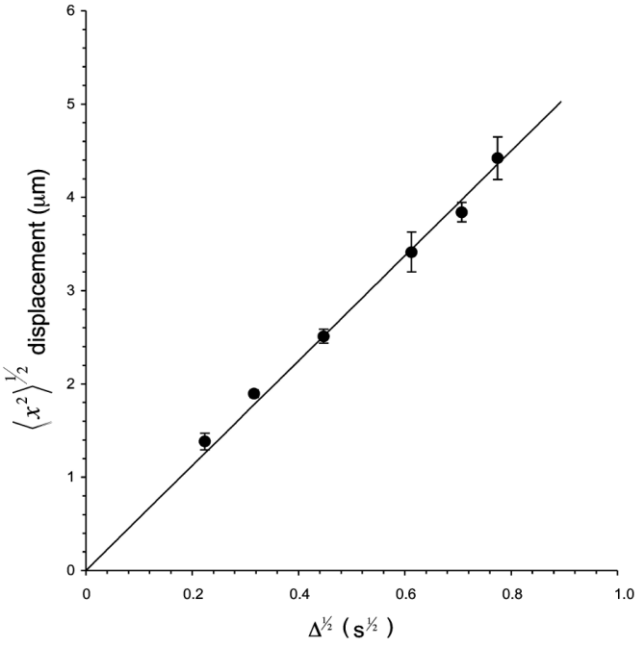

Figure 18. Conventional bicelles (DMPC/DHPC, q = 3.5) show a linear relationship between lipid displacement and the square root of diffusion time, consistent with free diffusion. Error bars reflect the fit uncertainty (±2σ) of the diffusion constant for each point.

When confined diffusion occurs, the measured diffusion constant decreases with diffusion time, as more molecules encounter the boundary. Figure 17a shows the diffusion measurement of lipids in 1.5/1.5/1/13 mol % bicelles at 292 K, in which the diffusion time, Δ, was 50 ms. As the diffusion time increases to 700 ms (Figure 17a–c), the measured self-diffusion constant is reduced from 4.9×10^{-12} m^2s^{-1} to 1.5×10^{-12} m^2s^{-1}, demonstrating lipid confinement.

In Figure 19, the apparent displacement, $\langle x_{app}^2 \rangle^{1/2} = \sqrt{4D_{app}\Delta}$, is plotted as a function of the square root of diffusion time for three different temperatures. At 300 K, above the expected miscibility transition, the displacement varies linearly with the square root of diffusion time, indicating free diffusion with no confinement or boundaries as observed in the conventional bicelles (Figure 18). At 295 K, the displacement does not increase linearly with the square root of diffusion time, but rather plateaus at ~ 3.0 μm, indicating that the lipids are confined within a micrometer-scale region. At 292 K, the plateau is at ~ 2.6 μm, indicating that the areas of confinement decreased with temperature (Figure 19). The changes in diffusion at different temperatures are fully reversible and diffusion measurements made on other samples of the same composition gave results consistent with those presented here.

To extract the true diffusion constant and the domain size, the displacement at 292 K and 295 K can be fit to the following equation [45]:

$$\langle x^2 \rangle^{1/2} = r \sin\left(\frac{\sqrt{4D_{true}\Delta}}{r}\right), \tag{11}$$

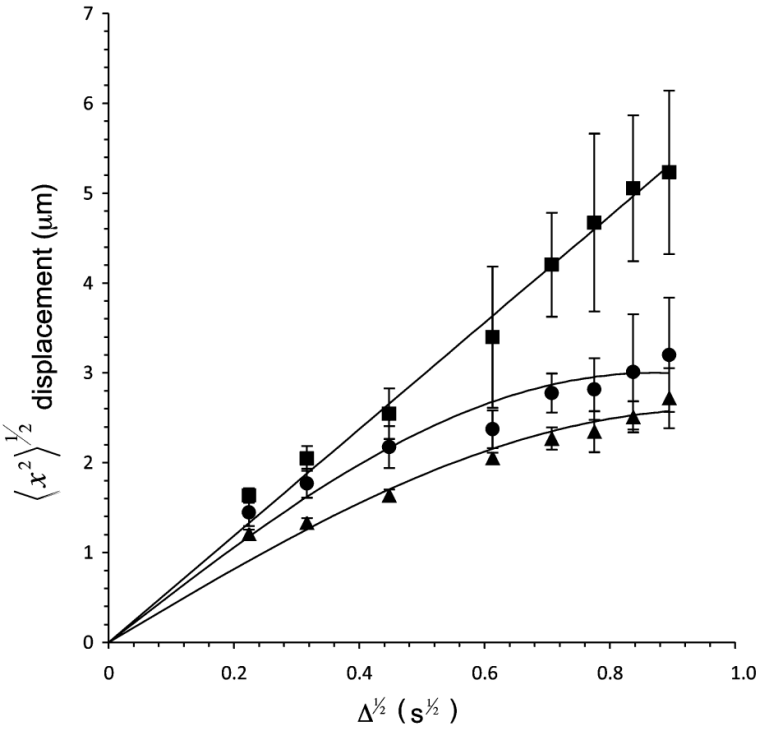

Figure 19. The average displacements in 1.5/1.5/1/chol DMPC/POPC/DHPC unsaturated lipid system with and without domains as a function of diffusion time at three temperatures. At 300 K (■), the displacement increased as the square root of time, consistent with free diffusion. In contrast, at temperatures 295 K (●) and 292 K (▲), the lipid displacements are limited and showed plateaus, indicating confined diffusion within a lipid domain. Error bars reflect the fit uncertainty ($\pm 2\sigma$) of the diffusion constant for each point.

which reduces to the expression for free diffusion when the domain size, *r*, is much larger than the displacement. The true diffusion constant at 292 K is $4.3 \pm 1.8 \times 10^{-12}$ m^2s^{-1} and $7.3 \pm 2.6 \times 10^{-12}$ m^2s^{-1} at 295 K (Table 1).

The composition of the domains is likely l_d. The size of the domain increases with temperature, consistent with l_d domains, and the domains disappear above the T_m of DMPC. Interestingly, our ^{1}H NMR spectrum of 1.5/1.5/1/13 mol % bicelles shows narrow (~ 45 Hz) lipid resonances that increase in intensity from 273 K to 310 K as the bicelles align. Previous ^{1}H MAS NMR spectroscopy of similar ternary lipid mixtures (DPPC, DOPC, and cholesterol) showed narrow acyl peaks (~ 50 Hz) for l_d domains, similar to our spectra, showing the same basic temperature dependence. However, we observed no signal from the l_o phase, while they observed broad (~1 kHz) peaks for l_o domains [92]. At these temperatures, the l_o phase is a very small fraction of the membrane and such a weak, broad peak was likely too small to detect.

This POPC/DMPC bicelle system exhibited micrometer-scale lipid domains, while vesicular systems of POPC/DMPC have shown no domains [93]. In previous work, it was speculated that the asymmetry of the POPC legs decreased its rotational mobility, and hindered formation of the l_o phase [93]. Bicelles exhibit greater lateral and rotational fluidity of the bicelle bilayer than vesicles [94], apparent in the scaled ^{31}P chemical shift anisotropy of the phosphatidylcholine head group, which might affect or favor the formation of domains. The presence of the amphiphile DHPC could play a role in the phase separation directly by partitioning into the bilayer, or the properties of the membrane as a whole simply by stabilizing perforations in the bilayer. Further work characterizing the domain formation in this model membrane, particularly the role of DHPC in domain formation, is described in Chapter 4.

Table 1. Diffusion constants and domain sizes in 1.5/1.5/1/13 mol % bicelle

sample temperature (K)	diffusion constant, D_{true} (10^{-12} m^2s^{-1})	domain size, r (μm)
292	4.3 ± 1.8	2.6 ± 0.4
295	7.3 ± 2.6	3.0 ± 0.3
300	8.8 ± 0.3	--

2.5 CONCLUSION

In this work, we created a uniaxially aligned membrane containing both saturated and unsaturated lipids, as well as cholesterol, capable of phase separating into lipid domains. Among the various model membranes we created, the 1.5/1.5/1/13 mol % molar ratios of DMPC/POPC /DHPC/cholesterol bicelles showed strong alignment over a large range of temperatures, and exhibited micrometer-scale phase separation into l_o and l_d domains, raising the possibility of structural studies of membrane proteins in domains and outside of domains. Structural biology studies of this sort could clarify the molecular action of membrane domains in cellular biology.

3.0 THE ROLE OF MEMBRANE PERFORATIONS IN THE ALIGNMENT OF BICELLES

3.1 ABSTRACT

Bicelles are valuable model membranes consisting of short chain lipids in the core that solvate perforations in the bilayer, and of long chain lipids that form a bilayer orienting in a magnetic field. Conventional bicelles, widely used in protein-related studies, consist of saturated long and short chain lipids. Any perturbations in the lipid composition can destroy the bicelle alignment. By clarifying the general alignment mechanism for bicelles of diverse composition, we hope to expand the diversity of model membranes available for membrane protein structural studies. We previously created a very stable bicelle containing cholesterol, saturated lipid and unsaturated lipid, and have compared the bilayer structure under alignment to that of conventional bicelles.

We used ^{31}P NMR to measure the density of perforations in the bilayer as a function of bicelle alignment and found a critical density for optimal bicelle alignment. While the temperature of optimal alignment differed for bicelles of different compositions, the perforation density was the same. The perforation density is a function of short chain lipid concentration, and the tendency of the short chain lipid to dissolve in the bilayer, reducing the number of perforations. We observed that bicelles showed a well-aligned structure when between ~ 65 %

and ~ 75 % of DHPC was forming perforations. As the temperature increased, the fraction of DHPC in the bilayer increased, depleting the number of perforations and destroying alignment. The fraction of DHPC in the core strongly correlated with the ability of bicelles of diverse compositions to align. Based on these results, it seems that the solubility of DHPC in the bilayer is a major limiting factor in the ability of any bicelles to align. We expect that understanding of role of DHPC for the bicelle alignment will help us predict and understand the alignment behavior and temperatures for bicelles with novel composition, reducing the hit-or-miss nature of novel bicelle creation.

3.2 INTRODUCTION

Cell membranes are a main structural element of living organisms and participate in various biological functions such as the conductance of ions and cell signaling [63, 95]. The biological membrane consists of the phospholipid bilayers, myriad proteins and cholesterol, and the dynamic interaction of these components has been widely studied to elucidate their biological function in living organisms [96, 97]. In particular, the physical and biochemical properties of proteins in the membranes have been well studied when reconstituted with artificial model membranes [98-100]. A model membrane retaining a few essential components of the complex cell membrane can allow the folding and activity of a membrane protein. Bicelles are one popular model membrane employed for structure and dynamics studies of membrane proteins because of their ability to orient in a magnetic field [62], and they have been used in most solid state NMR structural studies of transmembrane proteins [17, 49, 63-68]. Because membrane

structure and dynamics are easily affected by the lipid composition of the membrane, it is important to create an optimized model membrane for each biological system [50, 51].

In spite of the advantages mentioned above, it has been challenging to utilize a customized model membrane system in this field of research because the stability of bicelles is so sensitive to their composition. Difficulty in dealing with bicelles with their delicate nature has caused most people to utilize the simplest bicelle, composed of only saturated long and short chain lipid. However, it is hard to represent the cell membrane properties due to the simple composition of the model membrane compared to a cell membrane. Therefore, realization of a new model membrane often requires optimization of the preparation conditions and a process of trial and error to make the desired model. In order to predict and choose the aligned bicelles appropriate for the purposes of experiments using bicelles, it is necessary to understand the properties of the bicelles and their organizing principles for the alignment.

Bicelles are often idealized as perfectly segregating the long and short chain lipids into the bilayer and core, respectively. The ability of conventional bicelles to align has been correlated with the presence of perforations in the bilayer. We seek to generalize this correlation by quantifying the degree of perforation in unique aligned bicelles with a very different composition from conventional bicelles.

In addition, we have developed the use of ^{1}H NMR as a metric for bicelle alignment. Most studies about the morphology of bicelle focus on the observation of ^{31}P NMR spectra, because the chemical shift of the phosphorus head group reveals the orientation of the lipid in the magnetic field, and can monitor morphological changes at critical transition temperatures, including alignment. In our work, we measured the impact of bulk bilayer morphology on the ^{1}H NMR of the lipids. Observing phase behavior with ^{1}H NMR allows simultaneous observation of

sample alignment and spectroscopy of biological samples like proteins in the bilayer, requiring no additional experiments or equipment (^{31}P NMR probe). ^{1}H NMR measurements of bicelle alignment allow *in situ* measurements of bilayer phase when carrying out spectroscopy on proteins in the bicelle sample.

3.3 EXPERIMENTAL SECTION

3.3.1 SAMPLE PREPARATION

1,2-dimyristoyl-*sn*-glycero-3-phosphatidylcholine (DMPC, 99 %) in powder form, 1,2-di-o-hexyl-*sn*-glycero-3-phosphatidylcholine (DHPC, 99 %) in chloroform, and 1-palmitoyl-2-oleoyl-*sn*-glycero-3-phosphatidylcholine (POPC) in chloroform were purchased from Avanti Polar Lipids (Birmingham, AL). Lipids were used as purchased without further purification. Cholesterol (ovine wool, > 98 %) in powder form, 4-(2-hydroxyethyl)-1-piperazineethane sulfonic acid (HEPES, ≥ 99.5 %) and sodium azide were purchased from Sigma-Aldrich (Allentown, PA). Deuterium oxide was purchased from Cambridge Isotopes Lab (Woburn, MA).

The lipids were dissolved in chloroform and combined in a molar ratio of 1.5/1.5/1, 2/2/1 and 2.5/2.5/1 molar ratios of DMPC/POPC/DHPC with 13mol% cholesterol (calculated with respect to moles of long chain lipids) to create unsaturated bicelles with molar ratio, q = [DMPC]/[DHPC], equal to 3, 4, and 5 respectively. The lipid mixtures were placed under a nitrogen gas flow for ~ 20 minutes to remove chloroform and then placed on a vacuum line for at least 4 hours until the sample was reduced to a powder or powder/film mixture. A mixture of 10% deuterium oxide and water was added to each unsaturated bicelle sample to a concentration

of 30 % w/w. Three cycles of the following were performed: heating at 40 °C for 15 min, vortexing for 2 min, cooling at 0 °C for 15 min and again vortexing for 2 min, were performed to form bicelle mixtures. A 20 mM HEPES buffer (pH = 7.1) was used to redissolve the conventional bicelle mixture to a concentration of 30 % w/w. The same sequence of activities was again performed in three cycles.

3.3.2 NMR EXPERIMENTS

All spectra were acquired using an 11.7 T magnet with a Bruker Avance console (Bruker Biospin, Billerica, MA) and BCU05 Variable Temperature Control Unit. All sample rotors were 200 μL Bruker 4 mm ZrO_2 magic-angle spinning (MAS) rotors.

A 4 mm HXY MAS probe, was used to acquire the ^{31}P NMR spectra. All ^{31}P experiments were performed under static conditions. The variable temperature ^{31}P experiments at 201.67 MHz used FLOPSY at 6 kHz [84] for proton decoupling. The temperature was varied from 269 K to 320 K with the sample equilibrating in the probe for 10 to 15 minutes at each temperature. The ^{31}P chemical shifts were referenced to 85% phosphoric acid.

A high-resolution HCN HR-MAS probe (Bruker Biospin, Billerica, MA) was used to acquire the ^{1}H NMR spectra. All ^{1}H experiments were performed under MAS at 5 kHz in order to obtain isotropic spectra. ^{1}H spectra were acquired after temperature equilibration for 15 minutes. The variable temperature ^{1}H experiments were recorded at 500.12 MHz with WATERGATE for water suppression. The maximum gradient strength of the magic angle gradient coil was 0.513 T/m. The ^{1}H chemical shifts were referenced to H_2O at 298 K.

3.4 RESULTS AND DISCUSSION

3.4.1 PREDICTION OF BICELLE ALIGNMENT USING ^{31}P NMR SPECTRA: CORRELATING PERFORATION DENSITY AND BICELLE ALIGNMENT

In order to see the correlation between perforations and bicelle alignment, we prepared the series of the bicelle samples with different ratios of short and long chain lipids. By varying the concentration of short chain lipid (DHPC), we created bicelle samples with varying density of perforations. Using ^{31}P NMR, we could measure the alignment of each bicelle sample at a given temperature, and measure the concentration of DHPC in the core, reflecting the perforation density. In conclusion, by tracing the movement of the chemical shift of each component, we can understand the composition and structure of bicelles at each phase.

3.4.1.1 MEASURING PHASE DIAGRAM OF BICELLES WITH DIFFERENT q

We measured ^{31}P NMR spectra from q = 3 bicelles (Figure 20a) and q = 5 bicelles (Figure 20b) at temperatures from 267 K to 325 K. Representative ^{31}P spectra of each q showed how chemical shifts of peaks of short chain lipids (DHPC, blue) and long chain lipids (DMPC and POPC, green) move in the range of alignment. The alignment ranges of q = 3 and 5 are from 294 K to 306 K, and from 290 K to 300 K, respectively. At low temperatures, the lipids are in a gel phase, and the ^{31}P NMR has a chemical shift (δ) near 0 ppm. When the bicelles align in the magnetic field, the single peak of the gel splits into two peaks, reflecting the separation of long and short chain lipids into the bilayer and core region. The two distinguishable peaks of the long and short chain lipids are a direct marker of bilayer alignment. The peaks shift further apart after

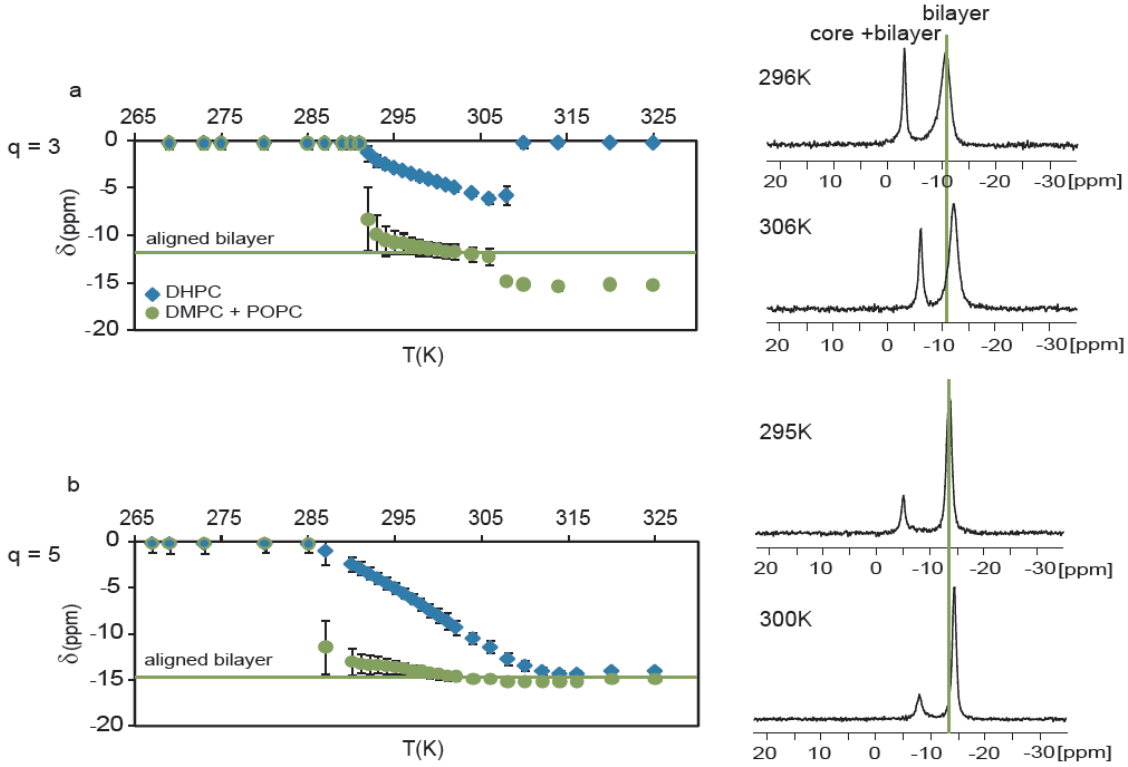

Figure 20. (a) The chemical shift of ^{31}P spectra of q = 3 of DMPC/POPC/DHPC/cholesterol bicelles respectively as a function of temperature and the representative ^{31}P spectra at 296 K and 306 K. (b) The chemical shift of ^{31}P spectra of q = 5 of DMPC/POPC/DHPC/cholesterol bicelles respectively as a function of temperature and the representative ^{31}P spectra at 295 K and 300 K. As temperature increases, the chemical shift of the DHPC peak (◆) moves toward the chemical shift of the long chain lipids (●) in an aligned bilayer (—) which is perpendicular to magnetic field. The error bar reflects the uncertainty of full width of half maximum (FWHM) due to the signal to noise.

the second phase transition from aligned bicelles to vesicles. As temperature increases, more DHPC partitions from the core into the bilayer. For q = 5, at the temperatures higher than 300 K all DHPC has entered the bilayer, resulting in a single ^{31}P peak at ~-15 ppm, arising from phosphocholine headgroups in the bilayer. For q = 3, the higher relative concentration of DHPC means that at high temperatures, excess DHPC is seen in a peak at 0 ppm reflecting micelles outside the bilayer, while a peak arising from DHPC, DMPC, and POPC in the bilayer is present at ~-15 ppm. In conclusion, the ^{31}P chemical shift offers a direct measure of the phase behavior of bicelles with different degrees of perforation.

3.4.1.2 PREDICTING ALIGNMENT FROM COMPOSITION OF BILAYER AND ε

Above T_m of bicelles, DHPC is present in both the core and bilayer environments, and exchanges rapidly between them. As temperature increases, DHPC increasingly incorporates into the bilayer, as it is shown by the continuous shift of the DHPC peak from the isotropic value (0 ppm) toward the chemical shift of the long chain lipids in the bilayer. The schematic cartoon in Figure 21a illustrates the partitioning of DHPC into the lipid bilayer plane. The increased partitioning of DHPC molecules into the bilayer depletes the number of perforations, and eventually the bicelle alignment ends. Figure 21b shows the upfield shift of the resonance frequency of the peak of DHPC and the peak of the long chain lipids, toward the aligned bilayer frequency. These shifts arise from two different phenomena. The chemical shift of the long chain lipids approaches the chemical shifts of a static lipid perpendicular to the magnetic field, reflecting the greater membrane rigidity and alignment at higher temperature. The chemical shift of DHPC, δ_{short}, also shifts upfield due to the greater alignment, but experiences an additional

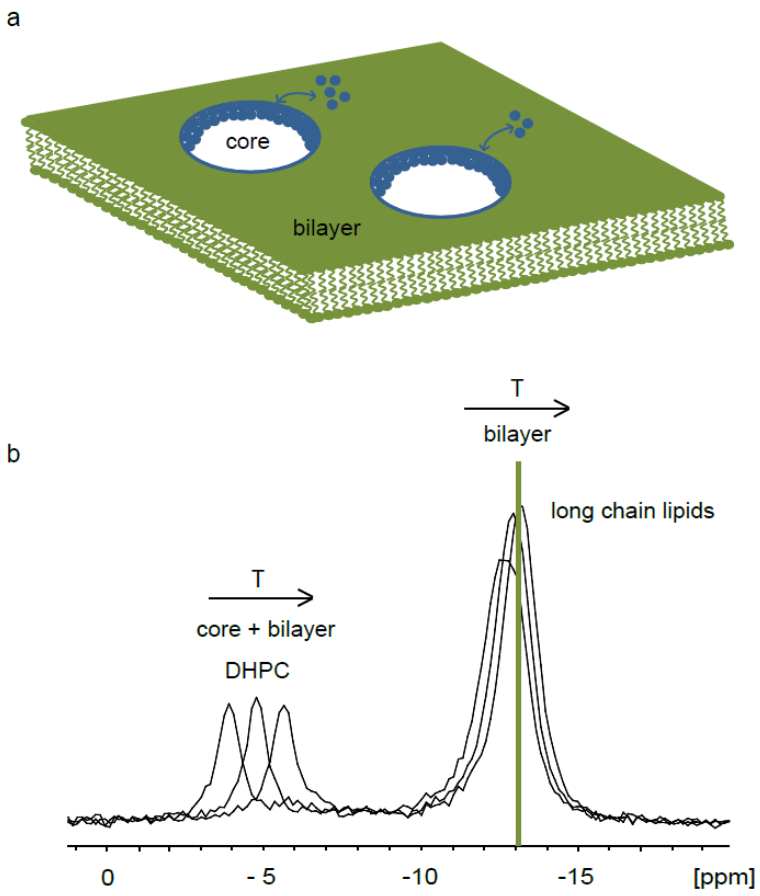

Figure 21. (a) The schematic cartoon of bilayer when DHPC (blue) partitions into long chain lipids (green)-rich plane. With the increased amount of DHPC in the bilayer plane, the bicelle will undergo a phase change from liquid crystal to vesicle. (b) As temperature increases, both the peaks of short chain lipids and long chain lipids in the low field shift to the high field. Since DHPC partitioning increases as the temperature increases, the DHPC peak moves closer to the long chain lipid peak consisting of the bilayer. While long chain lipids showed a slight shift to an aligned bilayer (—) due to the increase in overall alignment, DHPC shifted largely due to increased partitioning into the bilayer plane.

shift because of the increase in DHPC in the bilayer, reflected in Eq. (13).

$$\delta_{short} = \left(N_{DHPC}^{bilayer} \times \delta_{bilayer} + N_{DHPC}^{core} \times \delta_{core}\right)/N_{DHPC}^{total}\,, \tag{13}$$

where $\delta_{bilayer}$ and δ_{core} are the chemical shift of DHPC in bilayer and core, and are approximately equal to ~-15 ppm and ~ 0 ppm, respectively.

In order to elucidate the amount of DHPC in the bilayer and the core, the position of the DHPC peak, δ_{short} (referenced to the isotropic chemical shift, δ_{iso}) is plotted as a function of q. To remove the effect of the alignment on the DHPC chemical shift, the change in the peak position is normalized with respect to the shift observed for the long chain lipids ($\Delta\delta_{long}$). The ratio of the shifts, $\Delta\delta_{short}/\Delta\delta_{long} = (\delta_{short} - \delta_{iso}) / (\delta_{long} - \delta_{iso})$, reflects the effect of chemical exchange on the chemical shift and has removed the alignment contribution to shift.

From Eq. (13), we can derive the following equation relating the chemical shift to q:

$$\frac{\Delta\delta_{short}}{\Delta\delta_{long}} = \left(1 - \frac{\delta_{core}}{\delta_{bilayer}}\right)\frac{\varepsilon}{1-\varepsilon}q + \frac{\delta_{core}}{\delta_{bilayer}} = c_1 \cdot q + c_2\,, \tag{14}$$

where $\varepsilon = N_{DHPC}^{bilayer}/(N_{DHPC}^{bilayer} + N_{long}^{bilayer})$, the DHPC fraction of lipids in the bilayer [16, 101]. With perfect segregation of long and short chain lipids ε = 0, and increases as more DHPC partitions into the bilayer. In Figure 22, the ratio of $\Delta\delta_{short}/\Delta\delta_{long}$ is plotted as a function of q in the bicelle alignment temperature range. At each temperature, it was observed that $\Delta\delta_{short}/\Delta\delta_{long}$ proportionally increased with q, and that for a given q, $\Delta\delta_{short}/\Delta\delta_{long}$ increased with temperature. The linearity of the chemical shift with q shows that the partitioning of DHPC into the bilayer (ε)

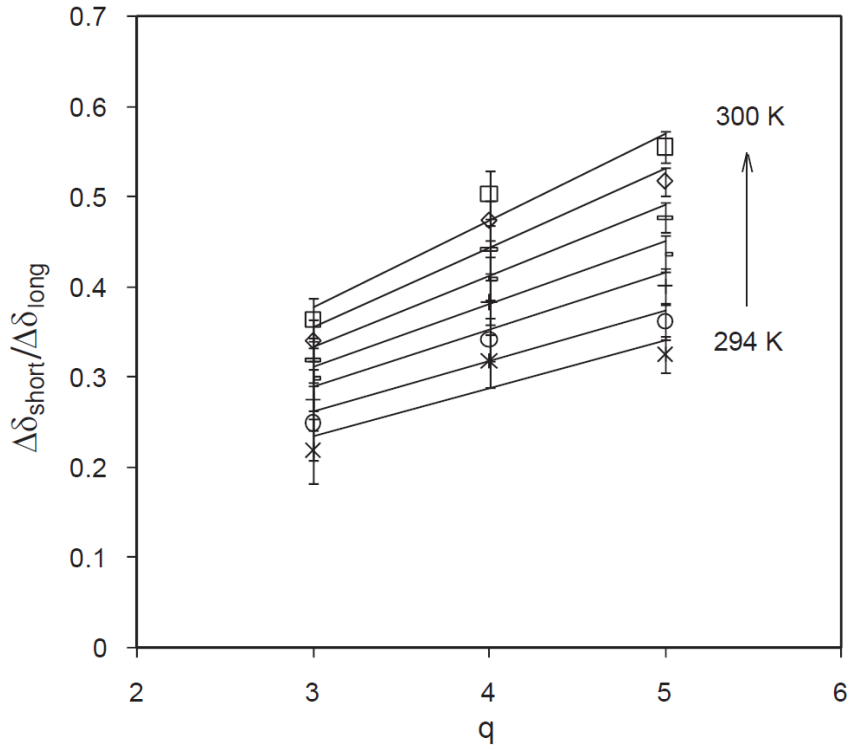

Figure 22. The plot of the ratio of $\Delta\delta_{short}/\Delta\delta_{long}$ as a function of q in the alignment temperature range. The measured temperatures are 294 K (✱), 295 K (o), 296 K (✚), 297 K (▬), 298 K(▬), 299 K (◇) and 300 K (□), respectively. At each temperature, $\Delta\delta_{short}/\Delta\delta_{long}$ proportionally increases with q and the $\Delta\delta_{short}/\Delta\delta_{long}$ at each q rises with increases in temperature. The error bar reflects the uncertainty of the chemical shift measurements due to the signal to noise.

is independent of q and changes only with the temperature.

As temperature increases, the ε increases at a given q, which means the fraction of DHPC partitioning into the bilayer from core is increasing. By fitting this data to Eq. (14), we extract ε for temperatures between 294 K and 300 K. From the value of ε we can calculate the fraction of DHPC in the core and bilayer environment. In order to know the fraction of DHPC in the bilayer at temperatures outside of this range, we exploit the Boltzmann distribution.

$$\varepsilon \propto e^{-\frac{E_a}{k_B T}}, \tag{15}$$

where k_B is Boltzmann constant and E_a is the partitioning energy of DHPC in bilayer. Eq. (15) predicts a linear relationship between $ln\varepsilon$ and 1/T, seen in our data (Figure 23). Since ε is constant at the same temperature regardless of q, by extrapolating to other temperatures, we can estimate how many DHPC exist in the bilayer at a given temperature for any q.

Table 2 shows the fraction of DHPC in the core at different temperatures for various values of q. At 294 K, where bicelles of all q aligned in a magnetic field, from ~ 72 % to ~ 83 % of the total DHPC was located in the core. In particular, q = 4 and 5 bicelles had two narrow and symmetric ^{31}P peaks at this temperature, indicating that the alignment was strong and uniform when DHPC was between ~ 72 % and ~ 77 % of total DHPC. Later, in this chapter we discuss the relationship between alignment and peak linewidth. The ^{31}P linewidths of DHPC of q = 3, 4 and 5 were narrowest at 300 K, 295 K and 296 K, respectively, indicating the best alignments. At these temperatures, the percentage of DHPC of q = 3, 4 and 5 in the core were ~ 68 %, ~ 75 % and ~ 65 %, respectively (highlighted in Table 2). Therefore, it is possible to conclude that when between ~ 65 % and ~ 75 % of the DHPC exists in the core, the bicelle will achieve a

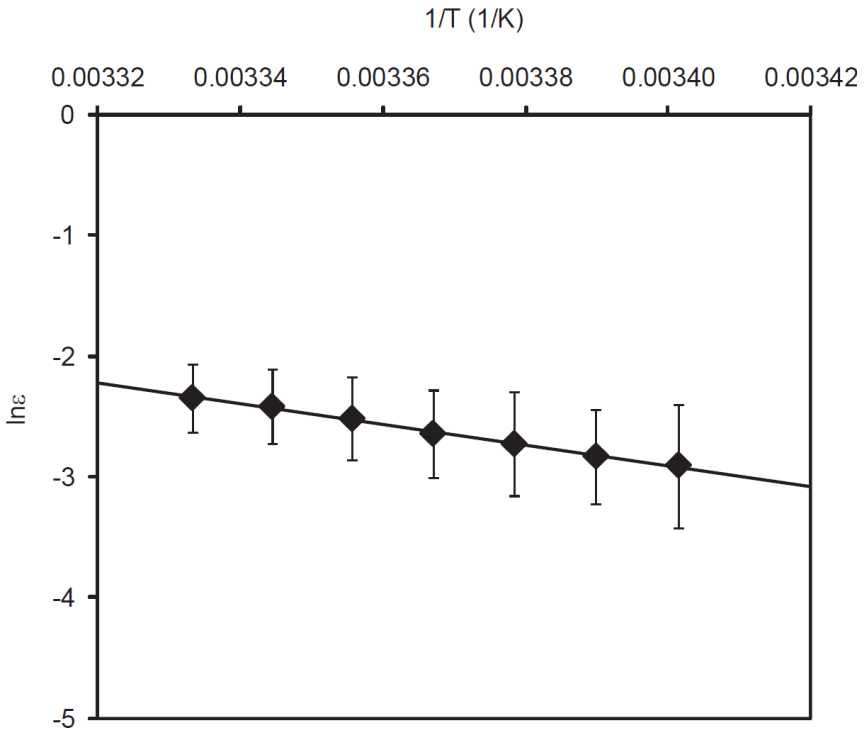

Figure 23. The natural log of fraction of DHPC in the bilayer plane (ε) is proportional to the inverse of temperature. Because the ε is only a function of temperature, the number of DHPC molecules existing in the bilayer and at the edge of each q bicelle can be estimated at each temperature. The error bars reflect the experimental uncertainty, arising from the fits in Figure 22.

Table 2. The amounts of DHPC (= n_{core}/n_{total}) existing in the core at different temperatures, for unsaturated and conventional bicelles

DMPC:POPC:DHPC:chol	294 K	295 K	296 K	300 K	308 K
q = 3	~ 83 %	~ 81 %	~ 79 %	~ 68 %	~ 23 %
q = 4	~ 77 %	~ 75 %	~ 72 %	~ 57 %	~ 0 %
q = 5	~ 72 %	~ 69 %	~ 65 %	~ 47 %	~ 0 %
DMPC:DHPC* q = 3.5	-	-	-	~ 85 %	~ 70 %

*Values from published study of conventional bicelles [16]

The most uniform (or strongest) alignments are highlighted for q = 3 to 5 and correspond to ~ 70 % of DHPC in the core.

well-aligned structure. The end of the alignment range occurs when the fraction of the DHPC in the core drops below 60 %. This corresponds well with the results at 300 K, where q = 3 is well-aligned but the q = 4 and 5 are at the end of the alignment range and about to transition to the vesicle with the DHPC below 60 %. This correlation between the fraction of DHPC and the alignment is also observed in published work on conventional bicelles, which consist of DHPC and DMPC [16]. According to ε values of conventional bicelles reported previously, it is estimated that ~ 85 % of DHPC are present at the core at 300 K, where the conventional bicelle starts aligning. When a bicelle is optimally aligned at 308 K, approximately 70 % of DHPC exists in the core, consistent with the requirements for the alignment of our bicelles.

Interestingly, at a single temperature, the fraction of DHPC molecules in the bilayer differs for different q. Although the Boltzmann distribution dictates that the fraction of DHPC in the bilayer depends on the temperature alone, the larger amounts of long chain lipids in higher q allow more DHPC molecules to partition into the bilayer. This can be seen in Table 2 for the bicelles at 308 K, where q = 3 bicelles still have 23 % of the DHPC in the core, while q = 4 and 5 bicelles have no DHPC remaining in the core, and accordingly have no perforations.

The differences in depletion according to q can explain why the alignment range ends at the lower temperature for higher q than that of lower q bicelles. At the same temperature, the higher q bicelles have more DHPC molecules in the bilayer plane and fewer DHPC molecules in the core, creating perforations. This implies that the depletion in the amount of short chain lipids in the core can cause the collapse of the liquid crystal structure, and that the composition of long and short chain lipids in the bilayer is correlated with alignment capability and morphology. The ε of our membranes is different from that of conventional bicelles at the same temperature due to the different bilayer composition. In the unsaturated bicelles, the ε value is larger than in

conventional bicelles (0.096 *vs* 0.04 at 300 K, respectively) [16], reflecting the larger solubility of the DHPC in a membrane with the unsaturated lipid and cholesterol. Accordingly, the fraction of the DHPC in the core is depleted at a lower temperature for the unsaturated bicelles, and their alignment range ends at a lower temperature than that of conventional bicelles (306 K *vs* 311 K, respectively).

3.4.1.3 OBSERVING THE CHANGE OF ^{31}P PEAK LINEWIDTHS OF DHPC AT PHASE TRANSITION

As we measured the ^{31}P NMR spectrum of bicelles at temperatures ranging from low to high, we noted the changes in the linewidth reflecting the critical changes in phase from gel to liquid crystal to vesicles. Since the location and molecular environment of the DHPC depends strongly on temperature, the line broadening of the DHPC peak was more sensitive than that of long chain lipids. Figure 24 shows the line widths of the DHPC peak in the ^{31}P NMR spectra of an assortment of bicelles as a function of temperature. The alignment range of each bicelle is described by a box. The linewidth showed similar trends in all of the bicelles. As shown in Figure 24a, the linewidth of the single ^{31}P peak containing both long and short chain lipids, from 269 K to 291 K is approximately 200 Hz, reflecting that the bicelles are in the gel phase. As the temperature approaches the T_m (= 292 K), the linewidth increases to the largest value of ~ 332 Hz at the T_m. The linewidth reaches another peak of over 400 Hz as the bicelles transition to vesicles. Major phase transitions are clearly seen in the ^{31}P linewidth.

Between the T_m and T_v phase transitions, the linewidth decreases to a minimum and then increases. The ^{31}P peak linewidth is a heterogeneous sum of peaks from bilayer with the range of directors. Immediately after T_m, highly perforated bilayers begin to align in the magnetic field. The membrane regions between the perforations are quite small and the orientation of their

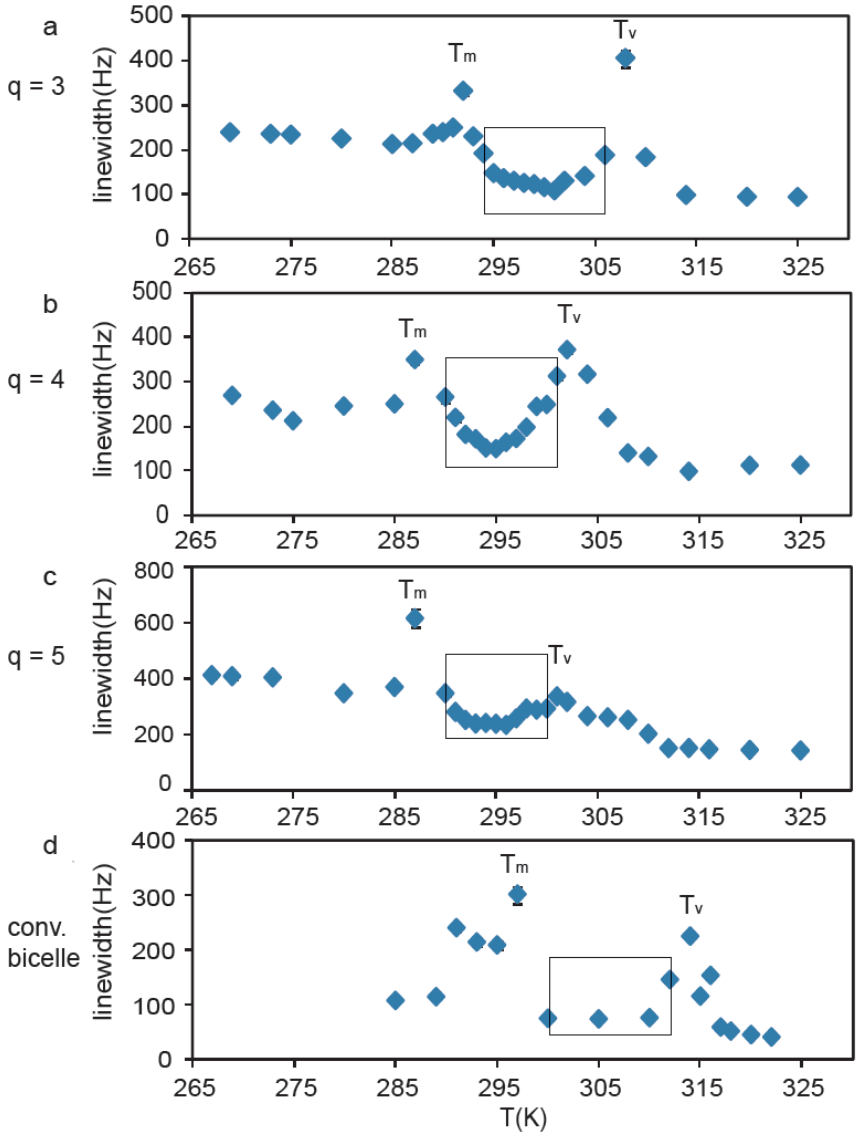

Figure 24. The plot of the linewidth of the low field peak from DHPC (◆) in ^{31}P NMR spectra of q = 3, 4, 5 of DMPC/POPC/DHPC/cholesterol bicelle as well as conventional bicelle (DMPC/DHPC, q = 3.5) as a function of temperature. Phase transitions are clearly seen in the change of ^{31}P linewidth. The error bar reflects the uncertainty of full width of half maximum (FWHM) due to the signal to noise.

membrane normal is able to fluctuate in the magnetic field with thermal motion. As temperature increases, the number of pores decreases, and the bigger membrane regions orient more strongly in the magnetic field. As the extent of bilayers increases, the range of director orientations decreases, narrowing the linewidth of the ^{31}P peak to its narrowest value, corresponding to the most homogeneous alignment. As the bilayer extent between perforations gets even larger, the membrane begins to bend, beginning the transition to vesicles. The bending again corresponds to a range of bilayer directors and exhibits an associated linebroadening [102]. The ^{31}P linewidth is more sensitive to the alignment and phase transition than the ^{31}P chemical shift. For example, in Figure 20b, the end of alignment for q = 5 is difficult to pick out. In contrast, Figure 24c shows a peak in the linewidth at 300 K, corresponding to the end of the alignment.

3.4.2 CAPABILITY OF THE OBSERVATION OF THE PHASE TRANSITION USING ^{1}H SPECTRA

As we explained above, the chemical shift and linewidth of the phosphorus spectrum give information about molecular structure, phase and alignment range. This fact led us to investigate if we could acquire such information looking at the ^{1}H NMR spectra, allowing us to use the same probe to take ^{1}H NMR of protein and membrane alignment in the same spectrum. Therefore, we measured the ^{1}H spectra of q = 3, 4 and 5 as the temperature was increased from 267 K to 315 K. The ^{1}H spectra were obtained under magic angle spinning and WATERGATE was applied to suppress the water peak at 4.7 ppm.

Figure 25 shows the changes in linewidth of three different peaks corresponding to double bond, acyl, and methyl moiety at the end of an acyl chain, which representatively exhibits significant changes in width as a function of temperature. As temperature increases, the

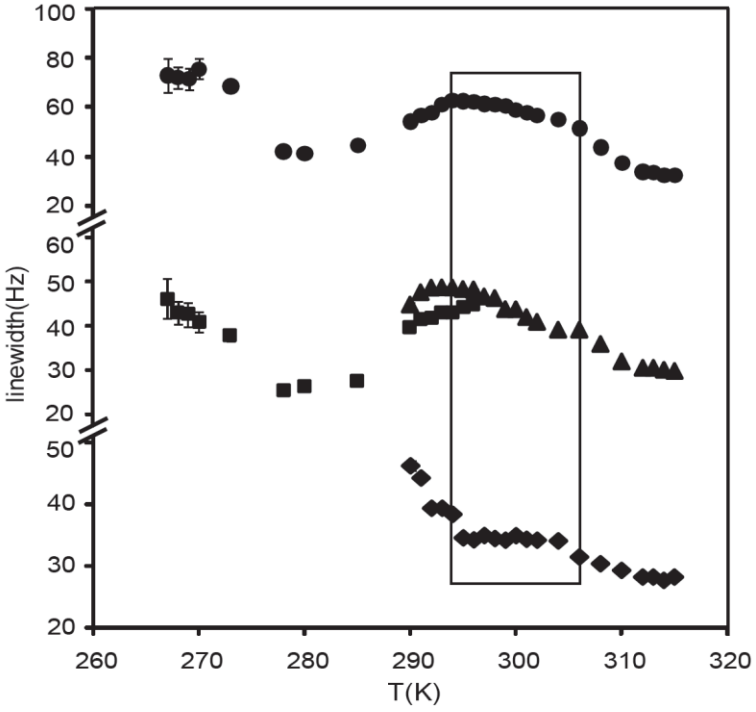

Figure 25. The changes of linewidths of ^{1}H NMR peaks are associated bicelle the phase transition and bicelle alignment. The plot shows the linewidths of double bond of unsaturated lipid (◆), acyl (●) and methyl at the end of acyl chain (■ and ▲) of q = 3 bicelle as a function of temperature from 267 K and 315 K. The box indicates the alignment range. When the error bar is smaller than the data point, it is not shown.

linewidths of all peaks varied, showing considerable changes near the point of the phase transition from gel to liquid crystal and from liquid crystal to vesicle form. The peak of the double bond (◆) appears right before T_m = 292 K, where bicelle transitions from gel to liquid crystal and the linewidth gets narrow after broadening as they align. The acyl (●) and methyl peaks (■ and ▲) also broaden as they start to align and become narrow with temperature increase. The methyl peak starts splitting near T_m into two peaks which then merge into one peak as the bicelle aligns. The linewidths of all these peaks suddenly get very narrow as soon as alignment of the bicelle finished and show relatively narrow and consistent values of about 30 Hz. Therefore, we can know that the change in ^{1}H linewidth is connected to the phase transition of the bicelle, and the linewidth of the methyl and the double bond peaks report the complex changes in the environment of these parts at critical moments such as alignment. However, the linewidths of acyl peaks of different q bicelles, shown in Figure 26, vary smoothly and continuously over the alignment range of the bicelles. For example, the ^{1}H acyl linewidth in a q = 5 bicelle decreases from ~ 75 Hz to ~ 30 Hz over the alignment range. The q = 3 bicelle peaks decrease from ~ 60 Hz to ~ 50 Hz in linewidth. The intense acyl ^{1}H peak therefore can report directly on the alignment state of a liquid crystal matrix while acquiring ^{1}H signal from a biological molecule embedded in the matrix. The homogeneous ^{1}H linewidth of the acyl chain reports the local dynamics and structure of the chain, not the overall alignment of the membrane. In contrast, the variation in ^{31}P linewidth in the alignment range indicates the heterogeneous nature of the peak, reflecting the various orientation of DHPC at critical temperatures.

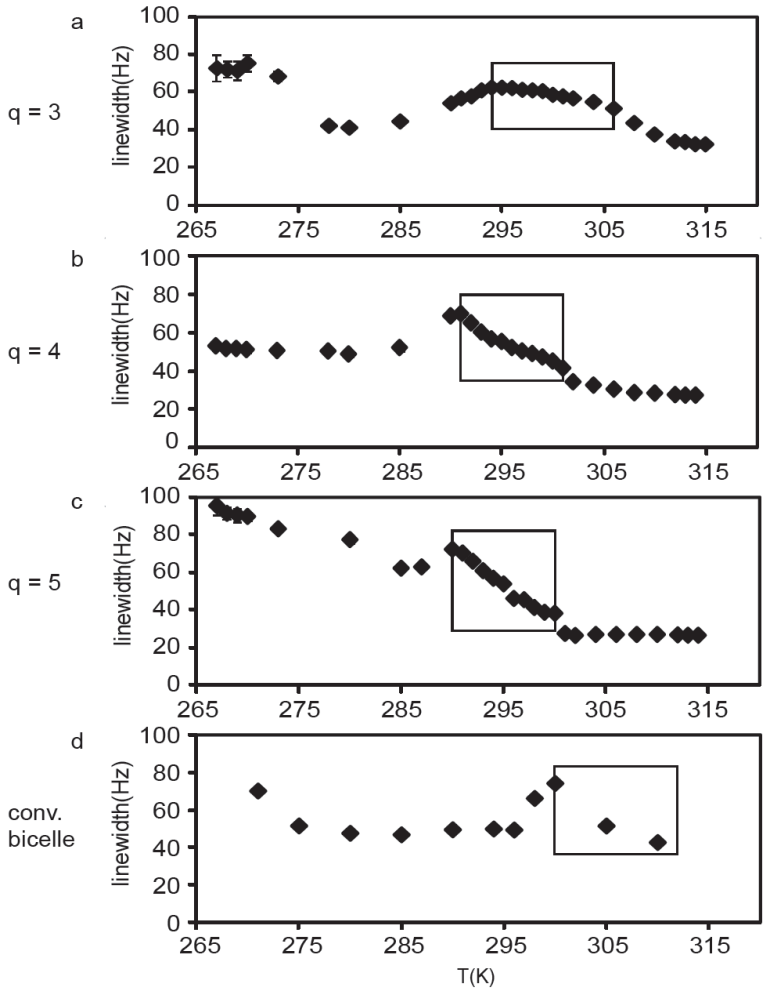

Figure 26. The plot of the ^{1}H linewidths of acyl peaks of q = 3, 4, 5 of DMPC/POPC/DHPC/ cholesterol bicelle as well as conventional bicelles as a function of temperature. The change of ^{1}H linewidth can be a criterion to identify the alignment range. The error bar reflects the uncertainty of full width of half maximum (FWHM) due to the signal to noise. When the error bar is smaller than the data point, it is not shown.

3.5 CONCLUSION

In this work, we observed the correlation of bilayer structure of diverse bicelle systems with their alignment capability, with the goal of clarifying the general alignment mechanism for bicelles of arbitrary composition. As previously reported, the bicelles will align above T_m when short chain lipids can mix with the long chain lipids. In order for planar bilayers to align, DHPC must form a significant density of pores in the bilayer. As temperature increases DHPC will migrate from pores to the bilayer, disrupting alignment. The larger the solubility of DHPC in the bilayer, the smaller the alignment range will be. The loss of alignment is gradual, as reflected by the ^{31}P linewidth, reaching completion at T_v. The solubility of DHPC in the long chain lipids may be able to be measured with vesicles composed of the long chain lipids, allowing a researcher to predict the ability of a given bicelle mixture to align.

The changes in chemical shift of ^{31}P NMR spectra showed the phase behavior of bicelles with different degrees of perforation, resulting in different phase diagram between q = 3 and 5. Moreover, the ^{31}P peak linewidth showed the alignment more clearly than simply the number of peaks and chemical shifts. The change in ^{1}H linewidth also could be used to characterize alignment, reflecting the dynamics of hydrocarbon chains of the lipids.

4.0 THE EFFECT OF MEMBRANE PERFORATION ON DOMAIN FORMATION AND BICELLE STRUCTURE

4.1 ABSTRACT

We have observed the formation of micron-scale domains in a bicelle containing a saturated lipid, DMPC, cholesterol, and an asymmetric unsaturated lipid, POPC (Chapter 2). However, Veatch and Keller reported that a vesicular system of DMPC/POPC/cholesterol had no micron-scale domains. It has been theorized that the tendency of POPC to partition to the interface of the l_o and l_d regions lowers the line tension of the interface and stabilizes nanoscopic domains. While vesicles and bicelles show similar physical properties, the bilayer in bicelles are highly perforated with stable holes created by DHPC. By varying the relative amounts of DHPC and long chain lipids (varying q) we were able to measure the effect of the perforation density on domain formation. The q = 3 bicelles, with a higher density of perforations, showed micron-scale domain formation, while the q = 5 bicelles, with a lower degree of perforation due to the smaller fraction of DHPC, showed no domains in NMR diffusion microscopy. The absence of domains of q = 5 correlates with the observation of no domains in the vesicular system with no perforations. Potentially, the interface of the bilayer and pore competes with the l_o–l_d interface for POPC, modulating the line tension at the domain interface. Using a geometric model for the bicelle structure, we calculated the surface density of pores, σ_p, and the distance between pores,

d_p, in both the q = 3 and q = 5 bicelles. From these calculations, we showed that the total length of the pore interface is ten times larger than the boundary length of a one micron domain for q = 5, and hundred times larger than the boundary length of a one micron domain for q = 3, allowing substantial depletion of POPC at the domain boundary. It is the first observation of membrane topology controlling domain formation, and is consistent with the theorized role of POPC as a line–active lipid.

4.2 INTRODUCTION

Domains in cell membranes are correlated with many biological functions such as signaling, transportation and association of proteins [29, 103, 104]. However, it is estimated that the cell membrane domain sizes are generally small, ~ 10 – 200 nm [29], and it makes the direct detection using optical spectroscopy difficult [105]. In order to understand the role of domains in the cell membrane, model membranes with ternary compositions of cholesterol, saturated lipids and unsaturated lipids are widely used to study domains, but domains in model systems are micron-scale, orders of magnitude larger than the cell membrane domains [61, 83]. The discrepancy in biological and model membrane domain sizes is not understood. Possible mechanisms are numerous and could involve the high density of membrane proteins in the cellular membrane (Figure 27) [30], the local curvature of the membrane [106-108], or the presence of a cytoskeleton [109, 110]. Interestingly, micron-scale domains are generally not observed when asymmetric legged lipids like POPC are the unsaturated component, although these are most similar to the lipids present in cellular membranes. For example, previous experimental results also showed that the vesicular ternary systems of saturated phosphocholine

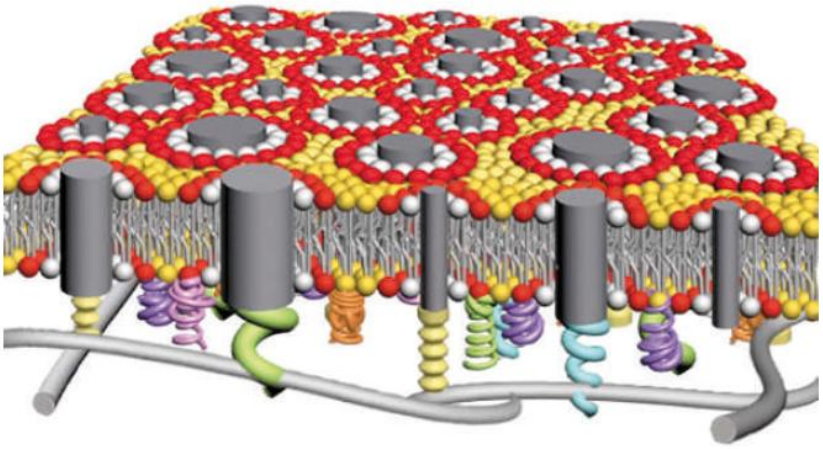

Figure 27. The schematic of the biological membrane with membrane proteins [30]. The density of membrane proteins in the cell is estimated to be ~ 30,000 /μm^2, creating a highly interrupted bilayer. Figure was taken from the reference [30].

lipids such as DMPC and symmetric unsaturated lipids such as DOPC (1,2-dioleoyl-*sn*-glycero-3-phosphocholine) with cholesterol showed the domain formation of micron-size [93]. However, the mixture of saturated phosphocholine lipids and asymmetric phosphocholine lipids such as POPC did not form domains [93].

The difference in the ability of symmetric and asymmetric lipids to form domains is of great interest. Generally, the size of domains can be explained in terms of line tension [111, 112]. The height mismatch of lipids in the l_o and l_d domains has an energetic cost called a line tension. As seen in Figure 28, asymmetric lipids like POPC can act as a line-active lipid, reducing the line tension in the interface of different domains by partitioning to those interfaces, leading to nanoscopic domains [111-114]. A high line tension drives the coalescence of smaller domains and results in micron-scale domains, while a low line tension leads to the formation of nanoscopic domains.

Instead of vesicular systems, bicelles, consisting of the planar bilayer and core, can be used as model membranes. Bicelles are very similar to vesicles, because the lateral diffusion of lipids [22, 83], the phase behavior [115, 116], and the transmembrane protein activity [49] are comparable with vesicles, and they show the same thicknesses of bilayer [71, 117]. Therefore, we expected to see the same basic domain formation in bicelles as in vesicles, and were surprised to see micron-scale domains in POPC-based bicelles when no such domains had been noted in the corresponding vesicles [93]. Bicelles and vesicles differ mainly in their degree of perforation, caused by the short chain lipid DHPC in bicelles. By decreasing the fraction of DHPC (increasing q), we reduced the degree of the perforations, creating model membranes more similar to the vesicles. Measuring the domain size in bicelles with different q will show the role of the perforations in domain formation. Models of the bicelle structure allow us to calculate

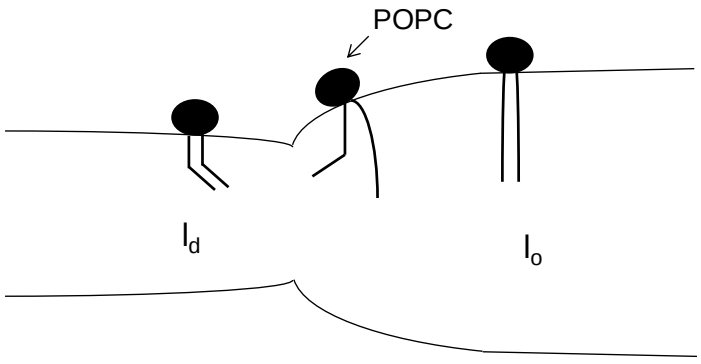

POPC

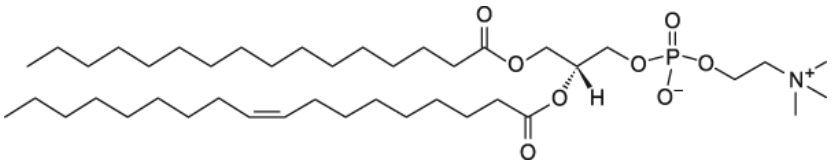

asymmetric (hybrid)

DOPC

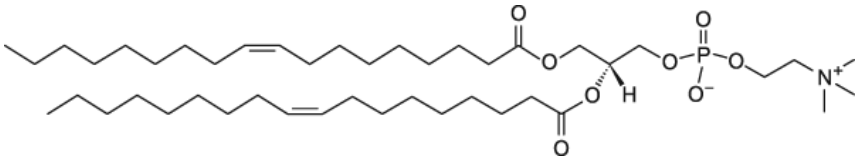

symmetric

Figure 28. The partitioning of the POPC in the interface of l_o and l_d domains. Different from the symmetric lipid, DOPC, POPC has asymmetric legs, which are partitioning in l_o and l_d, respectively. This lowers the line tension in the interface and results in the nanoscopic domain formation.

the surface density of pores in these bicelles of varying q, and quantitatively compare the interface between domains and the interface of the bilayer with the perforations. These models also allow us to compare the length of uninterrupted lipid expanse in the bicelles (the distance between the perforations) to that in the cell (the distance between membrane proteins), to examine the effect of nanoscopic structure on membrane properties.

4.3 RESULTS AND DISCUSSION

4.3.1 COMPARISON OF THE DOMAIN FORMATION IN q = 3 AND 5 BICELLES

To examine the effect of perforations on domain formations, we created bicelles with q = 3 (1.5/1.5/1/13 mol % ratios of DMPC /POPC/DHPC/cholesterol), and q = 5 (2.5/2.5/1/13 mol % of DMPC/POPC /DHPC/cholesterol). We carried out the experiments described in Chapter 2, measuring the lateral diffusion constant of the lipid in membrane as a function of the diffusion time. Any time-dependence of the diffusion constant served as a marker of domain formation. As described earlier, in free diffusion the lipid displacement will vary linearly with the square-root of diffusion time (Eq. 6).

$$\langle x^2 \rangle^{1/2} = \sqrt{4 D_{true} \Delta} \tag{6}$$

If domains are present, the displacement does not vary linearly with the square-root of diffusion time, and can be described by Eq. (11).

$$\langle x^2 \rangle^{1/2} = r \sin\left(\frac{\sqrt{4D_{true}\,\Delta}}{r}\right)$$

(11)

Figure 29a shows the results of the Chapter 2 for q = 3, in which the free diffusion is seen at 300 K, and confined diffusion seen at 292 K and 295 K when domains are present. Figure 29b shows the average displacements in the q = 5 bicelle system at three temperatures.

At 298 K, above the T_m of DMPC, q = 5 showed a linear relationship between lipid displacement and the square root of diffusion time, corresponding to the free diffusion. However, at 293 K and 294 K, where the formation of domains was noted for q = 3, the displacement also varied linearly with the square root of diffusion time, indicating the free diffusion. As described in Chapter 3, at a given temperature, the concentration of DHPC in the bilayer is the same for q = 3 and 5 due to the same ε, and only the number of DHPC molecules left in the core forming perforations differs. These results indicate that the formation of domains can be promoted or eliminated by modulating the concentration of DHPC in the core, and the density of the resulting perforations.

4.3.2 QUANTIFYING THE DIFFERENCE OF THE PERFORATIONS BETWEEN q = 3 AND 5

In order to analyze the relationship between the number of perforations and domain formation quantitatively, the geometric models of the bicelle structure allow the calculation of the pore density from the fraction of the DHPC molecules, and the membrane physical properties [118]. We calculated the surface density of pores, σ_p, and distance between pores, d_p of q = 3

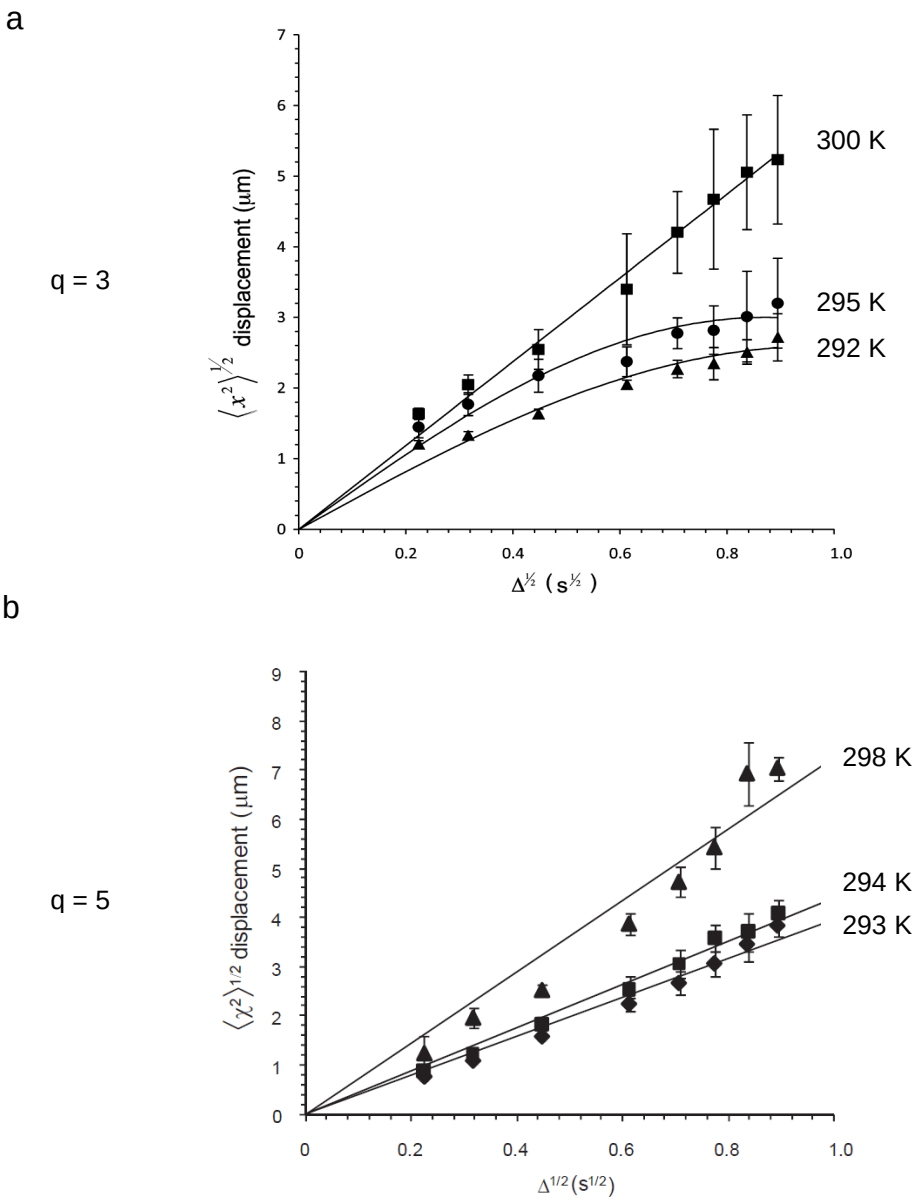

Figure 29. (a) The average displacements in q = 3 at 292 K (▲), 295 K (●), and 300 K (■). At 292 K and 295 K, the lipid displacements are limited and showed plateaus, indicating confined diffusion within a lipid domain. (b) The average displacements in q = 5 at 293 K (◆), 294 K (■), and 298 K (▲). Plots showed linear relationships between lipid displacement at each temperature and the square root of diffusion time, consistent with free diffusion without domains. Error bars reflect the fit uncertainty (±2σ) of the diffusion constant for each point.

and 5 bicelles at 295 K (highlighted in Table 3). The relative numbers of the DHPC molecules in the core and bilayer environments depend on the ε, as described in Chapter 3. The value of the ε for the q = 3 and q = 5 bicelles at 295 K is shown in Table 3. We can calculate the ratio of volumes of the entire bilayer and core using ε and the relative volumes of the long and short chain lipids, λ, as shown in Eq. (16) [93].

$$q_v = \frac{q}{\lambda}\left[\frac{1+\varepsilon(\lambda-1)}{1-\varepsilon(q+1)}\right], \tag{16}$$

where λ is the ratio between the volume of a short chain lipid and volume of a long chain lipid [71]. With the value of q_v, we can calculate the surface density of pores, σ_p, from Eq. (17) [119]

$$\sigma_p = \frac{6}{\pi(6R_p^2 + 3\pi q_v r_c R_p - 4q_v r_c^2)}, \tag{17}$$

where R_p is the pore size and r_c is the core thickness as can be seen in Figure 30. Since our model membrane used the same short chain lipid, DHPC, as conventional, we expect the same basic pore geometry and used the previously published values of ~ 400 Å and 44.2 Å for R_p and r_c, respectively [71, 117]. In a side note, the pore size in bicelles is similar to the pore size generated by electroporation on vesicles [120, 121].

We could then estimate the inter-pore distance, d_p, of both bicelles using σ_p because the pore density is correlated to the average of pore distance as shown in Eq. (18) [71].

$$d_p = \left(\sigma_p sin\frac{\pi}{3}\right)^{-\frac{1}{2}} - 2R_p \tag{18}$$

Table 3 . Difference in perforations of q = 3 and 5 at 295 K

q	ε	q_v	σ_p (pores/m^2)	d_p (nm)	hole-bilayer interface (μm)
3	0.059	~ 6.3	~ 1.32×10^{14}	~ 10	~ 100
5	0.059	~ 12.4	~ 1.04×10^{14}	~ 22	~ 75

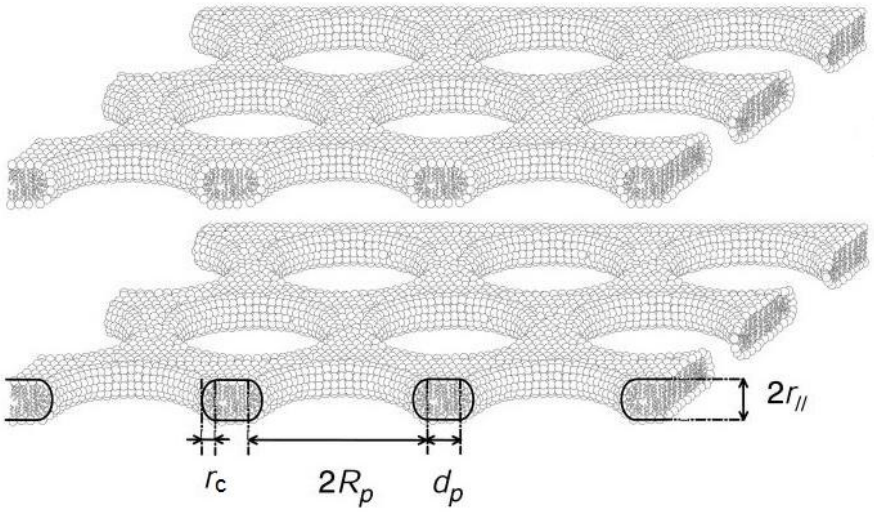

Figure 30. The schematic of perforated bilayer [71]. In this model membrane, the pore sizes are uniform. For calculations, previously reported values of R_p and r_c were used [71].

As seen in Table 3, when q was increased from 3 to 5, the surface density of pores was decreased from ~ 1.32×10^{14} pores/m^2 to ~ 1.04×10^{14} pores/m^2. The inter-pore distance is increased from ~ 10 nm to ~ 22 nm. As expected, as q is increased, the numbers of pores are decreased due to the depletion of DHPC in the membrane as shown in Figure 31.

We propose that the boundary of the perforations competes for POPC with the domain boundaries in Figure 32. Instead of POPC partitioning mainly to the domain boundaries, lowering the line tension [111, 112], and reducing the domain size [113, 122], the POPC is divided between the pore edges and the domain edges. This pore-induced redistribution of POPC results in the formation of large micron-scale domains. To reiterate, in q = 5, the lower density of pores allows more POPC to locate at the interface of l_o and l_d, leading to submicron domains similar to those seen in vesicles [113]. In q = 3, there are more POPC molecules associated with pores, and the line tension between l_o and l_d remains higher, leading to micron-scale domains. While changing the number of perforations by 30 % seems a subtle change, this corresponds to the order of magnitude change in the hole-bilayer interfacial length. The high density of pores means the one micron domain, with a circumference of ~ 6 μm will contain enough pores that the hole-bilayer interface will be approximately 100 μm for the q = 3 system (Table 3). In future work, we will measure the proximity of POPC to DHPC in the core to confirm this mechanism.

4.4 CONCLUSION

In this work, we observed the effect of the membrane perforation on domain formation.

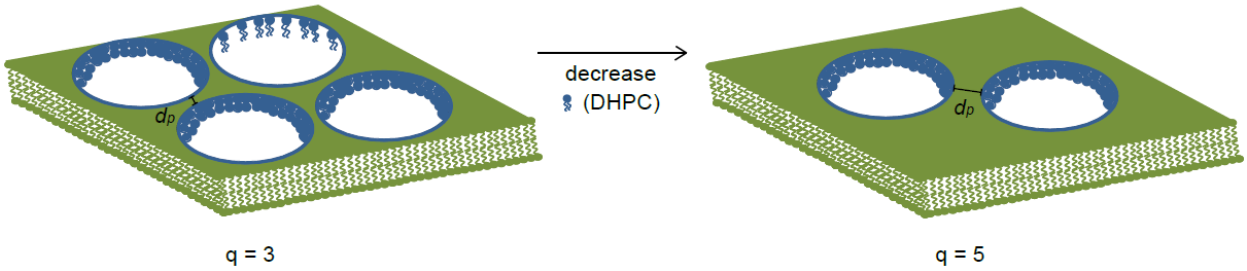

Figure 31. Increased q has fewer perforations and the longer distance of pores because of the decreased concentration of DHPC in the core.

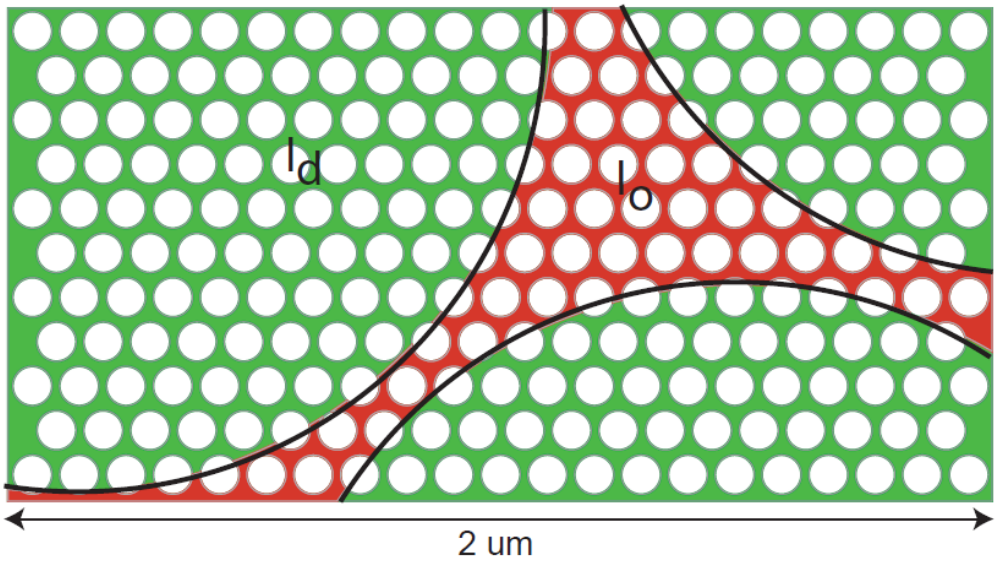

Figure 32. The boundary of the perforations competes for POPC with the domain boundaries. The hole-bilayer interface of ~ 100 μm (q = 3) redistributes POPC molecules, resulting in micron-scale domains. The rectangle is 2 μm by 1 μm, with 80 nm diameter pores, spaced 20 nm apart. The domains have a radius of 1 μm.

While q = 3 bicelles with many perforations showed the micron-scale domain formation, q = 5 bicelles with fewer perforations had no micron-scale domains. The lower concentration of perforations in q = 5 correlates with the lack of domains observed in vesicles with no perforation. The presence of perforations can have a significant impact on the spatial arrangement of lipids affecting bulk properties like line tension. Similarly, in the cell membrane, transmembrane proteins are densely packed and have a local density ten times that of the pores in the bicelles [30]. The high concentration of proteins in the bilayer could also actively modulate the spatial composition of the bilayer, with large effect.

5.0 CONCLUSION

In this work, we studied the structures in model membranes using solid state NMR and diffusion NMR techniques. We created a magnetically-aligned model membrane (bicelle) containing cholesterol and unsaturated lipids, with the goal of creating a versatile substrate for structural studies of transmembrane proteins with solid state NMR. The unsaturated bicelles exhibited micron-scale domains, measured by observation of time-dependent diffusion constants for lipid diffusing in the membrane. This NMR diffusion microscopy is a promising tool for the study of domains in model membranes and *in vivo*, examining the biological factors affecting domain formation, domain size, and domain dynamics.

There is a diversity of lipids in the cell, often correlating with particular membrane proteins. These membrane proteins need these lipids in any model membrane if a meaningful structure is desired. For example, the catalytic activity of diacylglycerol kinase (DAGK) was varied according to the model membrane system and also showed the different preference according the kinds of phosphocholine [73]. In order to understand the universal alignment mechanism of diverse bicelles, we observed the distribution of long and short chain lipids in the core and bilayer regions of the bicelles, correlating the distribution and the alignment capability. A critical fraction (~ 70 %) of DHPC must be located in the core for optimal alignment, regardless of the composition of the bilayer. The partitioning of DHPC into the bilayer results in the depletion of DHPC in the core, and the solubility of DHPC in the bilayer strongly affects the

alignment behavior. We hope that the measurement of the solubility of DHPC in vesicle of various compositions will enable us to forecast the alignment capability of novel bicelles.

Bicelles forming domains offer insight to the behavior of membranes with nanoscopic structure and variations in composition. We observed the effect of the membrane perforation on domain formation by creating series of bicelles with different density of perforations. The highly perforated bicelle showed micron-scale domain formation, but the less perforated bicelle showed no micron-scale domains. The change of topology affected the location of the line-active lipid, POPC, and led to a change in the line tension between domains enough to change the domain size. Similar mechanisms may occur in biological systems like cellular membranes.

APPENDIX A

[CALCULATION OF ERROR BARS]

A.1 ERRORS OF DIFFUSION CONSTANT

When diffusion experiment is performed by stimulated-echo pulsed field bipolar gradient diffusion experiment [104], the signal is attenuated with the variation of experimental parameters described by Stejskal Tanner equation [41]

$$\ln\left(\frac{I}{I_0}\right) = -\,g^2\gamma^2\delta^2\left(\Delta - \frac{\tau}{2} - \frac{\delta}{8}\right)\cdot D_{meas} = -k\cdot D_{meas}\ , \tag{12}$$

where I_0 is the acyl peak integral in the absence of gradients, τ is the spacing of the bipolar gradient pulses, and γ is gyromagnetic ratio for the observed nucleus. The attenuation of intensity depends on gradient duration δ, gradient amplitude g, and diffusion time Δ. We measured attenuation of signal intensity as g is increased. The measured diffusion constant D_{meas} can be calculated from a plot of $\ln(I/I_0)$ as a function of k. At that time, the reading of each attenuated intensity can have the measurement error by an uncertainty due to signal to noise ratio.

Therefore, we calculated the error of the measured signal intensity by using error propagation;

$$f = \frac{I}{I_0}$$

$$\left(\frac{\sigma_f}{f}\right)^2 = \left(\frac{\sigma_I}{I}\right)^2,$$

(A-1)

where σ_f is the error of the measured signal intensity and σ_I is the standard deviation of measured intensities of I due to noise of the spectrum. Therefore, (A-1) can be written as (A-2).

$$\left(\frac{\sigma_f}{f}\right)^2 = 2(1/SNR)^2$$

(A-2)

Finally σ_f can be calculated by (A-3), a rearrangement of (A-2),

$$\sigma_f = \sqrt{2}(1/SNR)\frac{I}{I_0}$$

(A-3)

and as a result, the error of signal, σ_f, can be obtained.

Then the uncertainty in $\ln\frac{I}{I_0}$, $\sigma_{\ln\frac{I}{I_0}}$, for each spectrum can be calculated by the error propagation as shown in (A-4).

$$\sigma_{\ln\frac{I}{I_0}} = \sigma_f \frac{I_0}{I}$$

(A-4)

The error bars shown in the plots of $\ln\frac{I}{I_0}$ *vs k* in Chapter 2 reflect the value of $\sigma_{\ln\frac{I}{I_0}}$. The error of measured diffusion constant, $\sigma_{D_{meas}}$, and the error of apparent diffusion constant, $\sigma_{D_{app}}$, reflect the standard deviation of the least-square fit of the data to a line.

In membranes where domains formed, a true diffusion constant, D_{true}, was extracted from the displacement as a function of diffusion time. The error of the true diffusion constant, $\sigma_{D_{true}}$, was extracted from the least-square fit to the following equation.

$$\langle x^2 \rangle^{1/2} = r\, sin\left(\frac{\sqrt{4D_{true}\,\Delta}}{r}\right) \tag{11}$$

Eq. (11) can be simply expressed to $<x^2>^{1/2} = Asin(B\Delta^{1/2})$ and we can obtain σ_A and σ_B directly from standard deviations measured from the simplified fitting Eq. (11). Since the domain size *r* is the same as A, the error of domain size σ_r is the regarded as σ_A. In order to obtain σ_{Dtrue} from Eq. (11), $B = 2D_{true}^{1/2}/r$ is rearranged to Eq. (A-5)

$$D_{true} = \frac{1}{4}r^2B^2\,, \tag{A-5}$$

and the error propagation can be applied to (A-5). The resulting σ_{Dtrue} can be given by Eq. (A-6).

$$\left(\frac{\sigma_{D_{true}}}{D_{true}}\right)^2 = \left(\frac{\sigma_{r^2}}{r^2}\right)^2 + \left(\frac{\sigma_{B^2}}{B^2}\right)^2 \tag{A-6}$$

The σ_r^2 and σ_B^2 can be written with σ_r and σ_B by the error propagations as shown in Eq. (A-7).

$$\sigma_r{}^2 = 2r\sigma_r$$

$$\sigma_B{}^2 = 2B\sigma_B$$

(A-7)

Finally, we obtained $\sigma_{D_{true}}$ of the confined diffusion by Eq. (A-8).

$$\sigma_{D_{true}} = 2D_{true}\sqrt{\frac{\sigma_r{}^2}{r^2} + \frac{\sigma_B{}^2}{B^2}}$$

(A-8)

If the membrane showed free diffusion without interruption, then $\sigma_{D_{true}}$ was calculated from the fitting, which is equal to Eq. (6), following Gaussian distribution.

$$\langle x^2 \rangle^{1/2} = \sqrt{4D_{true}\,\Delta}$$

(6)

Eq. (6) can be simply expressed to $\langle x^2 \rangle^{1/2} = A\Delta^{1/2}$ and A can be rearranged to get $D_{true} = A^2/4$. The error propagation to get $\sigma_{D_{true}}$ is given by Eq. (A-9).

$$\frac{\sigma_{D_{true}}}{D_{true}} = \frac{2\sigma_A}{A}$$

(A-9)

We can obtain σ_A directly from standard deviations measured from the simplified fitting Eq. (6). Finally, we can calculate $\sigma_{D_{true}}$ of the free diffusion by Eq. (A-10).

$$\sigma_{D_{true}} = \sigma_A\sqrt{D_{true}}$$

(A-10)

As seen in Eq. (6), the error of each displacement as a function of the square root of time reflects the error from the measured diffusion constant. The error of the displacement, $\sigma_{\langle x^2\rangle^{1/2}}$, was calculated from the fitting which is equal to Eq. (6), following Gaussian distribution. The error propagation to get $\sigma_{\langle x^2\rangle^{1/2}}$ is given by Eq. (A-11).

$$\frac{\sigma_{\langle x^2\rangle^{1/2}}}{\langle x^2\rangle^{1/2}} = \frac{1}{2}\frac{\sigma_{D_{meas}}}{D_{meas}} \tag{A-11}$$

Finally, we can get $\sigma_{\langle x^2\rangle^{1/2}}$ by Eq. (A-12) as a rearrangement of Eq. (A-11).

$$\sigma_{\langle x^2\rangle^{1/2}} = \frac{1}{2}\frac{\sigma_{D_{meas}}}{D_{meas}}\langle x^2\rangle^{1/2} \tag{A-12}$$

A.2 ERRORS OF THE NATURAL LOGARITHM OF ε

In Chapter 3, the error shown in the plot of $ln\varepsilon$ *vs* 1/T (Figure 23), $\sigma_{ln\varepsilon}$, is generated from the error of ε, σ_{ε}, and the error from the fitted data using Eq. (13).

$$\frac{\Delta\delta_{short}}{\Delta\delta_{long}} = \left(1 - \frac{\delta_{core}}{\delta_{bilayer}}\right)\frac{\varepsilon}{1-\varepsilon}q + \frac{\delta_{core}}{\delta_{bilayer}} = c_1 \cdot q + c_2 \tag{13}$$

The Eq. (13) can be rearranged to Eq. (A-13) as expressed by the relationship between ε, c_1, and c_2.

$$\varepsilon = \frac{c_1}{1 - c_2 + c_1}$$

(A-13)

The error of the obtained ε, σ_ε, is generated from the uncertainty of the value of c_1 and c_2. The σ_ε from Eq. (A-13) can be obtained using the error propagation.

$$\sigma_\varepsilon^2 = \frac{c_1^2}{(1 - c_2 + c_1)^2}\left[\left(\frac{\sigma_{c_1}}{c_1}\right)^2 + \left(\frac{\sigma_{1-c_2+c_1}}{1 - c_2 + c_1}\right)^2\right]$$

(A-14)

The $\sigma_{1-c_2+c_1}$ can be obtained from σ_{c_1} and σ_{c_2}, which are the standard deviations of c_1 and c_2, respectively. Therefore, σ_ε can be calculated from the Eq. (A-15).

$$\sigma_\varepsilon = \frac{c_1}{1 - c_2 + c_1}\sqrt{\frac{{\sigma_{c_1}}^2}{c_1^2} + \frac{{\sigma_{c_1}}^2 + {\sigma_{c_2}}^2}{(1 - c_2 + c_1)^2}}$$

(A-15)

Finally, from the obtained σ_ε, we can calculate $\sigma_{ln\varepsilon}$ as shown in Eq. (A-16).

$$\sigma_{ln\varepsilon} = \frac{\sigma_\varepsilon}{\varepsilon}$$

(A-16)

A.3 ERRORS OF THE CHEMICAL SHIFT MEASUREMENT

In the NMR spectrum, each peak has a Lorentzian shape. The Lorentzian line includes three factors which are the full width at half height (2λ) in ppm, amplitude (A), and peak distance from the center ($\Delta = X\text{-}X_0$) in ppm.

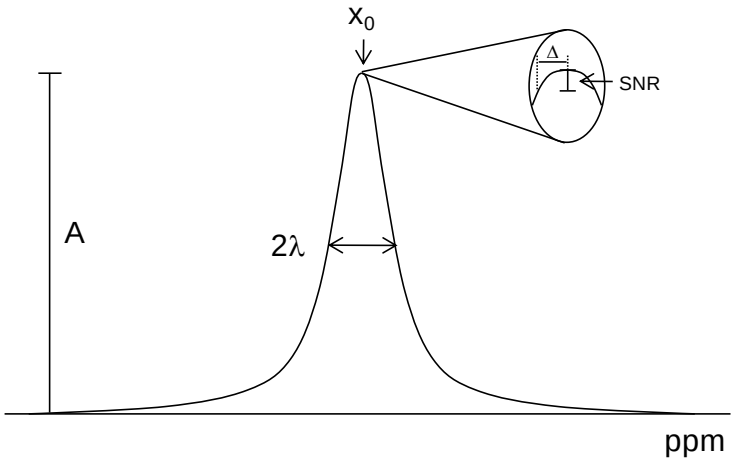

$$Y = A\frac{(2\lambda)^2}{(2\lambda)^2 + 4\Delta^2} \tag{A-17}$$

The accuracy of the measurement of chemical shift of the peak is dependent on how close the measured peak position is to the summit of the peak and the signal to noise ratio (SNR). A large SNR allows for a very precise location of the peak and a small error in the measurement of the chemical shift. Therefore, the relationship can be described as shown in (A-18).

$$Y(A) - Y(H) = noise\ , \tag{A-18}$$

where *Y(A)* is the position at summit of the peak and *Y(H)* is the measured peak position, respectively.

This equation (A-18) can be rearranged to (A-19) by Lorentzian equation.

$$1 - \frac{(2\lambda)^2}{(2\lambda)^2 + 4\Delta^2} = \frac{noise}{A} = \frac{1}{SNR}$$

(A-19)

This equation can be simplified as follows.

$$\frac{\lambda^2 + \Delta^2}{\lambda^2} = \frac{SNR}{SNR - 1}$$

$$\Delta = \lambda \sqrt{\frac{SNR}{SNR - 1} - 1}$$

(A-20)

The error of chemical shift measurement, σ_{cs}, takes place when there is a difference between λ and Δ. Therefore, the error can be expressed as shown in (A-21).

$$\sigma_{cs} = \lambda \left(1 - \sqrt{\frac{SNR}{SNR - 1} - 1} \right)$$

(A-21)

A.4 ERRORS OF THE LINEWIDTH MEASUREMENT

The error of the linewidth measurement, $\sigma_{\text{linewidth}}$, is caused by the difference between the real peak position of the full width at half height (2λ) and the peak position measured at the half height manually in Lorentzian shape. We assume that this error is a result of the SNR of this spectrum.

$$Y(H) - Y\left(\frac{A}{2}\right) = noise \tag{A-22}$$

It can be rewritten to (A-23) by the substitution into Lorentzian function

$$\frac{(2\lambda)^2}{(2\lambda)^2 + 4\Delta^2} - \frac{1}{2} = \frac{noise}{A} = \frac{1}{SNR}\,, \tag{A-23}$$

and it is summarized to (A-24).

$$\frac{\lambda^2 + \Delta^2}{\lambda^2} = \frac{2SNR}{2 + SNR}$$

$$\Delta = \lambda\sqrt{\frac{2SNR}{2 + SNR} - 1} \tag{A-24}$$

The $\sigma_{\text{linewidth}}$ arises when there is a difference between λ and Δ. Therefore, the error can be summarized as follows.

$$\sigma_{linewidth} = \lambda\left(1 - \sqrt{\frac{2SNR}{2 + SNR} - 1}\right)$$

(A-25)

BIBLIOGRAPHY

1. T.A. Cross and S.J. Opella, *Solid-state NMR structural studies of peptides and proteins in membranes.* Current Opinion in Structural Biology, 1994. **4**(4): p. 574-581.
2. S.J. Opella, P.L. Stewart, and K.G. Valentine, *Protein structure by solid-state NMR spectroscopy*. Quarterly Reviews of Biophysics, 1987. **19**(1-2): p. 7-49.
3. R.B. Klassen and S.J. Opella, *NMR Studies of Peptides and Proteins Associated with Membranes*. 1997. p. 271-297.
4. C.R. Sanders, B.J. Hare, K.P. Howard, and J.H. Prestegard, *Magnetically-oriented phospholipid micelles as a tool for the study of membrane-associated molecules.* Progress in Nuclear Magnetic Resonance Spectroscopy, 1994. **26**(Part 5): p. 421-444.
5. A. Watts, *Solid-state NMR in drug design and discovery for membrane-embedded targets.* Nat Rev Drug Discov, 2005. **4**(7): p. 555-568.
6. A. Watts, A.S. Ulrich, and D.A. Middleton, *Membrane protein structure: the contribution and potential of novel solid state NMR approaches (Review).* Molecular Membrane Biology, 1995. **12**(3): p. 233-246.
7. M. Rance, K.R. Jeffrey, A.P. Tulloch, K.W. Butler, and I.C.P. Smith, *Orientational order of unsaturated lipids in the membranes of Acholeplasma laidlawii as observed by 2H-NMR.* Biochimica et Biophysica Acta (BBA) - Biomembranes, 1980. **600**(2): p. 245-262.
8. W.L. Bragg, *The Analysis of Crystals by the X-ray Spectrometer.* Proceedings of the Royal Society of London. Series A, 1914. **89**(613): p. 468-489.
9. M.J. Duer, *Solid-State NMR Spectroscopy Principles and Applications.* 2002, Oxford: Blackwell Science.
10. E.R. Andrew, A. Bradbury, and R.G. Eades, *Nuclear Magnetic Resonance Spectra from a Crystal rotated at High Speed.* Nature, 1958. **182**(4650): p. 1659-1659.
11. R.R. Ketchem, W. Hu, and T.A. Cross, *High-resolution conformation of gramicidin A in a lipid bilayer by solid- state NMR.* Science, 1993. **261**(5127): p. 1457-1460.
12. B. Bechinger, Y. Kim, L.E. Chirlian, J. Gesell, J.M. Neumann, M. Montal, J. Tomich, M. Zasloff, and S.J. Opella, *Orientations of amphipathic helical peptides in membrane bilayers determined by solid-state NMR spectroscopy.* Journal of Biomolecular NMR, 1991. **1**(2): p. 167-173.
13. S.V. Dvinskikh, U.H.N. Durr, K. Yamamoto, and A. Ramamoorthy, *High-resolution 2D NMR spectroscopy of bicelles to measure the membrane interaction of ligands.* Journal of the American Chemical Society, 2007. **129**(4): p. 794-802.
14. G. Zandomeneghi, *Variable-angle spinning NMR techniques for the study of lipid bilayers and bilayer-associated peptides*. 2003, Zurich.

15. R.E. Minto, P.R. Adhikari, and G.A. Lorigan, *A 2H solid-state NMR spectroscopic investigation of biomimetic bicelles containing cholesterol and polyunsaturated phosphatidylcholine.* Chemistry and Physics of Lipids, 2004. **132**(1): p. 55-64.
16. M.N. Triba, D.E. Warschawski, and P.F. Devaux, *Reinvestigation by phosphorus NMR of lipid distribution in bicelles.* Biophysical Journal, 2005. **88**(3): p. 1887-1901.
17. A.A. De Angelis and S.J. Opella, *Bicelle samples for solid-state NMR of membrane proteins.* Nat. Protocols, 2007. **2**(10): p. 2332-2338.
18. D.D. Laws, H.-M.L. Bitter, and A. Jerschow, *Solid-State NMR Spectroscopic Methods in Chemistry.* Angewandte Chemie International Edition, 2002. **41**(17): p. 3096-3129.
19. F. Kramer, M.V. Deshmukh, H. Kessler, and S.J. Glaser, *Residual dipolar coupling constants: An elementary derivation of key equations.* Concepts in Magnetic Resonance Part A, 2004. **21A**(1): p. 10-21.
20. E.R. Andrew, A. Bradbury, and R.G. Eades, *Removal of dipolar broadening of nuclear magnetic resonance spectra of solids by specimen rotation.* Nature, 1959. **183**(4678): p. 1802-1803.
21. J. Klinowski, J. Hennel, and J. Klinowski, *Magic-Angle Spinning: a Historical Perspective,* in *New Techniques in Solid-State NMR*. 2005, Springer Berlin / Heidelberg. p. 1-14.
22. R. Soong and P.M. Macdonald, *Lateral diffusion of PEG-lipid in magnetically aligned bicelles measured using stimulated echo pulsed field gradient ^{1}H NMR.* Biophysical Journal, 2005. **88**(1): p. 255-268.
23. W.S. Price, *Pulsed-field gradient nuclear magnetic resonance as a tool for studying translational diffusion .1. Basic theory.* Concepts in Magnetic Resonance, 1997. **9**(5): p. 299-336.
24. W.S. Price, A.V. Barzykin, K. Hayamizu, and M. Tachiya, *A model for diffusive transport through a spherical interface probed by pulsed-field gradient NMR.* Biophysical Journal, 1998. **74**(5): p. 2259-2271.
25. Y. Cohen, L. Avram, and L. Frish, *Diffusion NMR Spectroscopy in Supramolecular and Combinatorial Chemistry: An Old Parameter—New Insights.* Angewandte Chemie International Edition, 2005. **44**(4): p. 520-554.
26. A. Pampel, J. Karger, and D. Michel, *Lateral diffusion of a transmembrane peptide in lipid bilayers studied by pulsed field gradient NMR in combination with magic angle sample spinning.* Chemical Physics Letters, 2003. **379**(5-6): p. 555-561.
27. L. Fielding, *NMR Methods for the Determination of Protein- Ligand Dissociation Constants.* Current Topics in Medicinal Chemistry, 2003. **3**: p. 39-53.
28. L. Fielding, *Determination of Association Constants (Ka) from Solution NMR Data.* Tetrahedron, 2000. **56**(34): p. 6151-6170.
29. L.J. Pike, *Rafts defined: a report on the Keystone symposium on lipid rafts and cell function.* Journal of Lipid Research, 2006. **47**(7): p. 1597-1598.
30. K. Jacobson, O.G. Mouritsen, and R.G.W. Anderson, *Lipid rafts: at a crossroad between cell biology and physics.* Nat Cell Biol, 2007. **9**(1): p. 7-14.
31. L.J. Pike, *The challenge of lipid rafts.* Journal of Lipid Research, 2009. **50**(Supplement): p. S323-S328.
32. M.A. Alonso and J. Millan, *The role of lipid rafts in signalling and membrane trafficking in T lymphocytes.* Journal of Cell Science, 2001. **114**(22): p. 3957-3965.

33. F.A. Heberle, J.T. Buboltz, D. Stringer, and G.W. Feigenson, *Fluorescence methods to detect phase boundaries in lipid bilayer mixtures.* Biochimica et Biophysica Acta (BBA) - Molecular Cell Research, 2005. **1746**(3): p. 186-192.
34. A. Yethiraj and J.C. Weisshaar, *Why are lipid rafts not observed in vivo?* Biophysical journal, 2007. **93**(9): p. 3113-3119.
35. K. Drbal, M. Moertelmaier, C. Holzhauser, A. Muhammad, E. Fuertbauer, S. Howorka, M. Hinterberger, H. Stockinger, and G.J. Schutz, *Single-molecule microscopy reveals heterogeneous dynamics of lipid raft components upon TCR engagement.* International Immunology, 2007. **19**(5): p. 675-684.
36. K. Simons and R. Ehehalt, *Cholesterol, lipid rafts, and disease.* The Journal of Clinical Investigation, 2002. **110**(5): p. 597-603.
37. M. Gandhavadi, D. Allende, A. Vidal, S.A. Simon, and T.J. McIntosh, *Structure, Composition, and Peptide Binding Properties of Detergent Soluble Bilayers and Detergent Resistant Rafts.* Biophysical journal, 2002. **82**(3): p. 1469-1482.
38. J.R. Silvius, *Role of cholesterol in lipid raft formation: lessons from lipid model systems.* Biochimica et Biophysica Acta (BBA) - Biomembranes, 2003. **1610**(2): p. 174-183.
39. A. Radhakrishnan and H.M. McConnell, *Condensed Complexes of Cholesterol and Phospholipids.* Biophys. J., 1999. **77**(3): p. 1507-1517.
40. S.L. Veatch, I.V. Polozov, K. Gawrisch, and S.L. Keller, *Liquid Domains in Vesicles Investigated by NMR and Fluorescence Microscopy.* Biophysical journal, 2004. **86**(5): p. 2910-2922.
41. R.M. Cotts, M.J.R. Hoch, T. Sun, and J.T. Markert, *Pulsed field gradient stimulated echo methods for improved NMR diffusion measurements in heterogeneous systems.* Journal of Magnetic Resonance (1969), 1989. **83**(2): p. 252-266.
42. P.T. Callaghan and O. Soderman, *Examination of the lamellar phase of aerosol OT/water using pulsed field gradient nuclear magnetic resonance.* J. Phys. Chem., 1983. **87**(10): p. 1737-1744.
43. E.O. Stejskal and J.E. Tanner, *Spin Diffusion Measurements: Spin Echoes in the Presence of a Time-Dependent Field Gradient.* The Journal of Chemical Physics, 1965. **42**(1): p. 288-292.
44. M.J. Saxton, *Modeling 2D and 3D Diffusion*. 2007. p. 295-321.
45. H.C. Gaede and K. Gawrisch, *Lateral diffusion rates of lipid, water, and a hydrophobic drug in a multilamellar liposome.* Biophysical Journal, 2003. **85**(3): p. 1734-1740.
46. M. Edidin, *The state of lipid rafts: From model membranes to cells.* Annual Review of Biophysics and Biomolecular Structure, 2003. **32**: p. 257-283.
47. H.A. Lucero and P.W. Robbins, *Lipid rafts-protein association and the regulation of protein activity.* Archives of Biochemistry and Biophysics, 2004. **426**(2): p. 208-224.
48. M. Caffrey, *Membrane protein crystallization.* Journal of Structural Biology, 2003. **142**(1): p. 108-132.
49. F.M. Marassi and S.J. Opella, *NMR structural studies of membrane proteins.* Current Opinion in Structural Biology, 1998. **8**(5): p. 640-648.
50. K. Boesze-Battaglia and R. Schimmel, *Cell membrane lipid composition and distribution: implications for cell function and lessons learned from photoreceptors and platelets.* J Exp Biol, 1997. **200**(23): p. 2927-2936.
51. G. van Meer, D.R. Voelker, and G.W. Feigenson, *Membrane lipids: where they are and how they behave.* Nat Rev Mol Cell Biol, 2008. **9**(2): p. 112-124.

52. S.R. Wassall, M.R. Brzustowicz, S.R. Shaikh, V. Cherezov, M. Caffrey, and W. Stillwell, *Order from disorder, corralling cholesterol with chaotic lipids: The role of polyunsaturated lipids in membrane raft formation.* Chemistry and Physics of Lipids, 2004. **132**(1): p. 79-88.
53. O. Bakht, P. Pathak, and E. London, *Effect of the Structure of Lipids Favoring Disordered Domain Formation on the Stability of Cholesterol-Containing Ordered Domains (Lipid Rafts): Identification of Multiple Raft-Stabilization Mechanisms.* 2007. **93**(12): p. 4307-4318.
54. A. Lee, *How Lipids Affect the Activities of Integral Membrane Proteins.* Biochim Biophys Acta, 2004. **1666**: p. 62-87.
55. S.H. Park and S.J. Opella, *Tilt Angle of a Trans-membrane Helix is Determined by Hydrophobic Mismatch.* Journal of Molecular Biology, 2005. **350**(2): p. 310-318.
56. K. Turnheim, J. Gruber, C. Wachter, and V. Ruiz-Gutierrez, *Membrane phospholipid composition affects function of potassium channels from rabbit colon epithelium.* Am J Physiol Cell Physiol, 1999. **277**(1): p. C83-90.
57. D. Schmidt, Q.-X. Jiang, and R. MacKinnon, *Phospholipids and the origin of cationic gating charges in voltage sensors.* Nature, 2006. **444**(7120): p. 775-779.
58. E. van den Brink-van der Laan, J. Antoinette Killian, and B. de Kruijff, *Nonbilayer lipids affect peripheral and integral membrane proteins via changes in the lateral pressure profile.* Biochimica et Biophysica Acta (BBA) - Biomembranes, 2004. **1666**(1-2): p. 275-288.
59. A. Ramamoorthy, D.-K. Lee, T. Narasimhaswamy, and R.P.R. Nanga, *Cholesterol reduces pardaxin's dynamics--a barrel-stave mechanism of membrane disruption investigated by solid-state NMR.* Biochimica et Biophysica Acta (BBA) - Biomembranes. **In Press, Corrected Proof**.
60. F. Tokumasu, A.J. Jin, G.W. Feigenson, and J.A. Dvorak, *Nanoscopic Lipid Domain Dynamics Revealed by Atomic Force Microscopy.* 2003. **84**(4): p. 2609-2618.
61. A. Filippov, G. Oradd, and G. Lindblom, *Domain Formation in Model Membranes Studied by Pulsed-Field Gradient-NMR: The Role of Lipid Polyunsaturation.* 2007. **93**(9): p. 3182-3190.
62. I. Marcotte, Auger, M., *Bicelles as model membranes for solid- and solution-state NMR studies of membrane peptides and proteins.* Concepts in Magnetic Resonance Part A, 2005. **24A**(1): p. 17-37.
63. A. Ramamoorthy, S.K. Kandasamy, D.-K. Lee, S. Kidambi, and R.G. Larson, *Structure, Topology, and Tilt of Cell-Signaling Peptides Containing Nuclear Localization Sequences in Membrane Bilayers Determined by Solid-State NMR and Molecular Dynamics Simulation Studies‚Ä†.* Biochemistry, 2007. **46**(4): p. 965-975.
64. S.K. Kandasamy, D.-K. Lee, R.P.R. Nanga, J. Xu, J.S. Santos, R.G. Larson, and A. Ramamoorthy, *Solid-state NMR and molecular dynamics simulations reveal the oligomeric ion-channels of TM2-GABAA stabilized by intermolecular hydrogen bonding.* Biochimica et Biophysica Acta (BBA) - Biomembranes, 2009. **1788**(3): p. 686-695.
65. A.A. De Angelis, S.C. Howell, A.A. Nevzorov, and S.J. Opella, *Structure determination of a membrane protein with two trans-membrane helices in aligned phospholipid bicelles by solid-state NMR spectroscopy.* Journal of the American Chemical Society, 2006. **128**: p. 12256-12267.

66. A.A. De Angelis, A.A. Nevzorov, S.H. Park, S.C. Howell, A.A. Mrse, and S.J. Opella, *High-Resolution NMR Spectroscopy of Membrane Proteins in Aligned Bicelles.* Journal of the American Chemical Society, 2004. **126**(47): p. 15340-15341.
67. A.A. De Angelis, *NMR experiments on aligned samples of membrane proteins.* Methods Enzymol., 2005. **394**: p. 350-382.
68. J. Xu, U.H.N. D¸rr, S.-C. Im, Z. Gan, L. Waskell, and A. Ramamoorthy, *Bicelle-Enabled Structural Studies on a Membrane-Associated Cytochrome b_5 by Solid-State MAS NMR Spectroscopy.* Angewandte Chemie International Edition, 2008. **47**(41): p. 7864-7867.
69. M. Ottiger and A. Bax, *Characterization of magnetically oriented phospholipid micelles for measurement of dipolar couplings in macromolecules.* Journal of Biomolecular NMR, 1998. **12**(3): p. 361-372.
70. R. Soong and P.M. Macdonald, *Influence of the long-chain/short-chain amphiphile ratio on lateral diffusion of PEG-lipid in magnetically aligned lipid bilayers as measured via pulsed-field-gradient NMR.* Biophysical Journal, 2005. **89**(3): p. 1850-1860.
71. M.N. Triba, P.F. Devaux, and D.E. Warschawski, *Effects of Lipid Chain Length and Unsaturation on Bicelles Stability. A Phosphorus NMR Study.* Biophys. J., 2006. **91**(4): p. 1357-1367.
72. M.A. Parker, V. King, and K.P. Howard, *Nuclear magnetic resonance study of doxorubicin binding to cardiolipin containing magnetically oriented phospholipid bilayers.* Biochimica et Biophysica Acta (BBA) - Biomembranes, 2001. **1514**(2): p. 206-216.
73. L. Czerski and C.R. Sanders, *Functionality of a Membrane Protein in Bicelles.* Analytical Biochemistry, 2000. **284**(2): p. 327-333.
74. H. Sasaki, S. Fukuzawa, J. Kikuchi, S. Yokoyama, H. Hirota, and K. Tachibana, *Cholesterol Doping Induced Enhanced Stability of Bicelles.* Langmuir, 2003. **19**(23): p. 9841-9844.
75. F.d.r. De Meyer and B. Smit, *Effect of cholesterol on the structure of a phospholipid bilayer.* Proceedings of the National Academy of Sciences, 2009. **106**(10): p. 3654-3658.
76. G. Lindblom, L.B.A. Johansson, and G. Arvidson, *Effect of cholesterol in membranes. Pulsed nuclear magnetic resonance measurements of lipid lateral diffusion.* Biochemistry, 1981. **20**(8): p. 2204-2207.
77. M. Edidin, *Rotational and Translational Diffusion in Membranes.* Annual Review of Biophysics and Bioengineering, 1974. **3**(1): p. 179-201.
78. H.C. Gaede and K. Gawrisch, *Lateral Diffusion Rates of Lipid, Water, and a Hydrophobic Drug in a Multilamellar Liposome.* Biophys. J., 2003. **85**(3): p. 1734-1740.
79. G. Lindblom and G. Oradd, *NMR studies of translational diffusion in lyotropic liquid crystals and lipid membranes.* Progress in Nuclear Magnetic Resonance Spectroscopy, 1994. **26**: p. 483-515.
80. A. Filippov, G. Oradd, and G. Lindblom, *Lipid Lateral Diffusion in Ordered and Disordered Phases in Raft Mixtures.* Biophysical Journal, 2004. **86**(2): p. 891-896.
81. G. Oradd, P.W. Westerman, and G. Lindblom, *Lateral diffusion coefficients of separate lipid species in a ternary raft-forming bilayer: A Pfg-NMR multinuclear study.* Biophysical Journal, 2005. **89**(1): p. 315-320.
82. I.V. Polozov, L. Bezrukov, K. Gawrisch, and J. Zimmerberg, *Progressive ordering with decreasing temperature of the phospholipids of influenza virus.* Nat Chem Biol, 2008. **4**(4): p. 248-255.

83. I.V. Polozov and K. Gawrisch, *Domains in binary SOPC/POPE lipid mixtures studied by pulsed field gradient H-1 MAS NMR.* Biophysical Journal, 2004. **87**(3): p. 1741-1751.
84. M. Kadkhodaie, O. Rivas, M. Tan, A. Mohebbi, and A.J. Shaka, *Broadband homonuclear cross polarization using flip-flop spectroscopy.* Journal of magnetic resonance, 1991. **91**(2): p. 437-443.
85. L.L. Latour, L.M. Li, and C.H. Sotak, *Improved PFG Stimulated-Echo Method for the Measurement of Diffusion in Inhomogeneous Fields.* Journal of Magnetic Resonance, Series B, 1993. **101**(1): p. 72-77.
86. J.E. Tanner, *Use of the Stimulated Echo in NMR Diffusion Studies.* The Journal of Chemical Physics, 1970. **52**(5): p. 2523-2526.
87. C.R. Sanders and J.P. Schwonek, *Characterization of magnetically orientable bilayers in mixtures of dihexanoylphosphatidylcholine and dimyristoylphosphatidylcholine by solid-state NMR.* Biochemistry, 1992. **31**: p. 8898-8905.
88. B. Alberts, Johnson, A., Lewis, J., Raff, M., Roberts, K. and Walter,P., *Molecular Biology of the Cell.* fourth edition ed. 2001, New York: Garland Science.
89. P.L. Yeagle, *Cholesterol and the cell membrane.* Biochimica et Biophysica Acta (BBA) - Reviews on Biomembranes, 1985. **822**(3-4): p. 267-287.
90. E. London, *Insights into lipid raft structure and formation from experiments in model membranes.* Current Opinion in Structural Biology, 2002. **12**(4): p. 480-486.
91. G. Zandomeneghi, P.T.F. Williamson, A. Hunkeler, and B.H. Meier, *Switched-angle spinning applied to bicelles containing phospholipid-associated peptides.* Journal of Biomolecular NMR, 2003. **25**(2): p. 125-132.
92. I.V. Polozov and K. Gawrisch, *Characterization of the Liquid-Ordered State by Proton MAS NMR.* Biophys. J., 2006. **90**(6): p. 2051-2061.
93. S.L. Veatch and S.L. Keller, *Separation of Liquid Phases in Giant Vesicles of Ternary Mixtures of Phospholipids and Cholesterol.* Biophys. J., 2003. **85**(5): p. 3074-3083.
94. C.R. Sanders and J.H. Prestegard, *Magnetically orientable phospholipid bilayers containing small amounts of a bile salt analogue, CHAPSO.* Biophys. J., 1990. **58**: p. 447-460.
95. S. Hagiwara, S. Miyazaki, and N.P. Rosenthal, *Potassium current and the effect of cesium on this current during anomalous rectification of the egg cell membrane of a starfish.* The Journal of General Physiology, 1976. **67**(6): p. 621-638.
96. G. Benga and R.P. Holmes, *Interactions between components in biological membranes and their implications for membrane function.* Progress in Biophysics and Molecular Biology, 1984. **43**(3): p. 195-257.
97. J. Seelig and A. Seelig, *Lipid conformation in model membranes and biological membranes.* Quarterly Reviews of Biophysics, 1980. **13**(01): p. 19-61.
98. L.T. Mimms, G. Zampighi, Y. Nozaki, C. Tanford, and J.A. Reynolds, *Phospholipid vesicle formation and transmembrane protein incorporation using octyl glucoside.* Biochemistry, 1981. **20**(4): p. 833-840.
99. F.N. Katz, J.E. Rothman, V.R. Lingappa, G.n. Blobel, and H.F. Lodish, *Membrane assembly in vitro: Synthesis, glycosylatio, and asymmetric insertion of a transmembrane protein.* Proceedings of the National Academy of Sciences, 1977. **74**(8): p. 3278-3282.
100. T. Nakae, *Identification of the outer membrane protein of that produces transmembrane channels in reconstituted vesicle membranes.* Biochemical and Biophysical Research Communications, 1976. **71**(3): p. 877-884.

101. C.R. Sanders and J.P. Schwonek, *Characterization of magnetically orientable bilayers in mixtures of dihexanoylphosphatidylcholine and dimyristoylphosphatidylcholine by solid-state NMR.* Biochemistry, 1992. **31**(37): p. 8898-8905.
102. R.R. Vold and R.S. Prosser, *Magnetically Oriented Phospholipid Bilayered Micelles for Structural Studies of Polypeptides. Does the Ideal Bicelle Exist?* Journal of Magnetic Resonance, Series B, 1996. **113**(3): p. 267-271.
103. M. Edidin, *THE STATE OF LIPID RAFTS: From Model Membranes to Cells.* Annual Review of Biophysics and Biomolecular Structure, 2003. **32**(1): p. 257-283.
104. L.J. Pike, *Lipid rafts.* Journal of Lipid Research, 2003. **44**(4): p. 655-667.
105. K. Simons and E. Ikonen, *Functional rafts in cell membranes.* Nature, 1997. **387**(6633): p. 569-572.
106. A. Iglic, H. Hägerstrand, P. Veranic, A. Plemenitas, and V. Kralj-Iglic, *Curvature-induced accumulation of anisotropic membrane components and raft formation in cylindrical membrane protrusions.* Journal of Theoretical Biology, 2006. **240**(3): p. 368-373.
107. R. Lipowsky, *Domains and Rafts in Membranes – Hidden Dimensions of Selforganization.* Journal of Biological Physics, 2002. **28**(2): p. 195-210.
108. K. Simons and W.L.C. Vaz, *Model systems, lipid rafts, and cell membranes* Annual Review of Biophysics and Biomolecular Structure, 2004. **33**(1): p. 269-295.
109. M. Villalba, K. Bi, F. Rodriguez, Y. Tanaka, S. Schoenberger, and A. Altman, *Vav1/Rac-dependent actin cytoskeleton reorganization is required for lipid raft clustering in T cells.* The Journal of Cell Biology, 2001. **155**(3): p. 331-338.
110. D. Holowka, E.D. Sheets, and B. Baird, *Interactions between Fc(epsilon)RI and lipid raft components are regulated by the actin cytoskeleton.* Journal of Cell Science, 2000. **113**(6): p. 1009-1019.
111. A.J. García-Sáez, S. Chiantia, and P. Schwille, *Effect of Line Tension on the Lateral Organization of Lipid Membranes.* Journal of Biological Chemistry, 2007. **282**(46): p. 33537-33544.
112. A.J. García-Sáez and P. Schwille, *Stability of lipid domains.* FEBS Letters, 2010. **584**(9): p. 1653-1658.
113. R. Brewster and S.A. Safran, *Line Active Hybrid Lipids Determine Domain Size in Phase Separation of Saturated and Unsaturated Lipids.* Biophysical journal, 2010. **98**(6): p. L21-L23.
114. Z.J.a.M. Wang, Deserno, *Systematic implicit solvent coarse-graining of bilayer membranes: lipid and phase transferability of the force field.* New Journal of Physics, 2010. **12**(9): p. 095004.
115. S.A. Johnson, B.M. Stinson, M.S. Go, L.M. Carmona, J.I. Reminick, X. Fang, and T. Baumgart, *Temperature-dependent phase behavior and protein partitioning in giant plasma membrane vesicles.* Biochimica et Biophysica Acta (BBA) - Biomembranes. **1798**(7): p. 1427-1435.
116. R.A. Parente and B.R. Lentz, *Phase behavior of large unilamellar vesicles composed of synthetic phospholipids.* Biochemistry, 1984. **23**(11): p. 2353-2362.
117. J.F. Nagle and S. Tristram-Nagle, *Structure of lipid bilayers.* Biochimica et Biophysica Acta (BBA) - Reviews on Biomembranes, 2000. **1469**(3): p. 159-195.

118. M.N. Triba, P.F. Devaux, and D.E. Warschawski, *Effects of lipid chain length and unsaturation on bicelles stability. A phosphorus NMR study.* Biophysical Journal, 2006. **91**(4): p. 1357-1367.
119. D.M. Small, *The physical chemistry of lipids: from alkanes to phospholipids*, ed. D.M. Small. 1986, New York: Plenum Press. 489-500 p.
120. E. Neumann and S. Kakorin, *Electrooptics of membrane electroporation and vesicle shape deformation.* Current Opinion in Colloid & Interface Science, 1996. **1**(6): p. 790-799.
121. S.A. Freeman, M.A. Wang, and J.C. Weaver, *Theory of electroporation of planar bilayer membranes: predictions of the aqueous area, change in capacitance, and pore-pore separation.* Biophysical journal, 1994. **67**(1): p. 42-56.
122. R. Brewster, P.A. Pincus, and S.A. Safran, *Hybrid Lipids as a Biological Surface-Active Component.* Biophysical journal, 2009. **97**(4): p. 1087-1094.